Article

Neuron

Caldendrin Directly Couples Postsynaptic Calcium Signals to Actin Remodeling in Dendritic Spines

Highlights

- Calcium binding relieves intra-molecular inhibition of caldendrin
- Caldendrin binding activates cortactin and promotes F-actin stabilization in spines
- Caldendrin depletion results in loss of stable F-actin and spine plasticity deficits
- Caldendrin directly couples $[Ca^{2+}]i$ to the stabilization of F-actin in synapses

Authors

Marina Mikhaylova, Julia Bär, Bas van Bommel, ..., Oliver Stork, Casper C. Hoogenraad, Michael R. Kreutz

Correspondence

marina.mikhaylova@zmnh.uni-hamburg.de (M.M.), michael.kreutz@lin-magdeburg.de (M.R.K.)

In Brief

Activity-dependent remodeling of the actin cytoskeleton is essential for synaptic plasticity. Mikhaylova et al. describe a novel molecular mechanism directly translating the initial calcium influx into coordinated rearrangement of spinous actin filaments at the nanoscale in dendritic spines.

Mikhaylova et al., 2018, Neuron *97*, 1110–1125
March 7, 2018
https://doi.org/10.1016/j.neuron.2018.01.046

CellPress

CellPress

Neuron
Article

Caldendrin Directly Couples Postsynaptic Calcium Signals to Actin Remodeling in Dendritic Spines

Marina Mikhaylova,[1,2,3,8,*] Julia Bär,[1,2,8] Bas van Bommel,[1] Philipp Schätzle,[3] PingAn YuanXiang,[2] Rajeev Raman,[2] Johannes Hradsky,[2] Anja Konietzny,[1] Egor Y. Loktionov,[4] Pasham Parameshwar Reddy,[2] Jeffrey Lopez-Rojas,[2] Christina Spilker,[2] Oliver Kobler,[5] Syed Ahsan Raza,[6] Oliver Stork,[6] Casper C. Hoogenraad,[3] and Michael R. Kreutz[2,7,9,*]

[1]Emmy Noether Group "Neuronal Protein Transport," Center for Molecular Neurobiology, ZMNH, University Medical Center Hamburg-Eppendorf, Hamburg 20251, Germany
[2]RG Neuroplasticity, Leibniz-Institute for Neurobiology, Magdeburg 39118, Germany
[3]Cell Biology, Faculty of Science, Utrecht University, Utrecht 3584 CH, the Netherlands
[4]State Lab for Photon Energetics, Bauman Moscow State University, Moscow 105005, Russia
[5]Combinatorial Neuroimaging Core Facility (CNI), Leibniz Institute for Neurobiology, Magdeburg 39118, Germany
[6]Institute of Biology, Otto von Guericke University, Magdeburg 39120, Germany
[7]Leibniz Group "Dendritic Organelles and Synaptic Function," Center for Molecular Neurobiology, ZMNH, University Medical Center Hamburg-Eppendorf, Hamburg 20251, Germany
[8]These authors contributed equally
[9]Lead Contact
*Correspondence: marina.mikhaylova@zmnh.uni-hamburg.de (M.M.), michael.kreutz@lin-magdeburg.de (M.R.K.)
https://doi.org/10.1016/j.neuron.2018.01.046

SUMMARY

Compartmentalization of calcium-dependent plasticity allows for rapid actin remodeling in dendritic spines. However, molecular mechanisms for the spatio-temporal regulation of filamentous actin (F-actin) dynamics by spinous Ca^{2+}-transients are still poorly defined. We show that the postsynaptic Ca^{2+} sensor caldendrin orchestrates nano-domain actin dynamics that are essential for actin remodeling in the early phase of long-term potentiation (LTP). Steep elevation in spinous $[Ca^{2+}]_i$ disrupts an intramolecular interaction of caldendrin and allows cortactin binding. The fast on and slow off rate of this interaction keeps cortactin in an active conformation, and protects F-actin at the spine base against cofilin-induced severing. Caldendrin gene knockout results in higher synaptic actin turnover, altered nanoscale organization of spinous F-actin, defects in structural spine plasticity, LTP, and hippocampus-dependent learning. Collectively, the data indicate that caldendrin-cortactin directly couple $[Ca^{2+}]_i$ to preserve a minimal F-actin pool that is required for actin remodeling in the early phase of LTP.

INTRODUCTION

Dendritic spine synapses undergo structural plasticity in an activity-dependent manner. A deeper appreciation of the underlying mechanisms will ultimately help to understand how information is stored at the cellular level. F-actin is highly enriched in spines and represents a key substrate for plasticity-related changes in spine morphology (Bosch et al., 2014; Honkura et al., 2008). Accordingly, it has been shown that the dynamics of actin polymerization and severing underlie the morphological changes caused by induction of LTP or long-term depression of synaptic transmission (Bosch and Hayashi, 2012; Matsuzaki et al., 2004; Rácz and Weinberg, 2013).

At hippocampal Schaffer-collateral CA1 synapses, Ca^{2+} influx through N-Methyl-D-aspartate receptors (NMDARs) is instructive for F-actin dynamics (Bosch et al., 2014; Kim et al., 2015; Okamoto et al., 2007). Current evidence suggests that a complex interplay between actin-binding proteins (ABPs) and upstream signaling cascades activates or inhibits actin polymerization, branching, and stabilization, in turn underlying the organization of F-actin in spines (Hotulainen and Hoogenraad, 2010; Kim et al., 2015). Several ABPs exhibit a dynamic association with spinous actin: they dissociate from and re-enter spines that undergo plasticity in a tightly controlled temporal manner (Bosch et al., 2014). Upon LTP induction, rapid spine entry of the F-actin severing protein cofilin-1 results in an increased number of barbed ends. F-actin branching (Arp2/3 complex) or capping (actin binding protein 1) proteins transiently increase, whereas ABPs involved in stabilizing the suprastructure of the actin cytoskeleton by bundling F-actin or linking F-actin to the postsynaptic density (PSD) are transiently reduced (Bosch et al., 2014; Okamoto et al., 2007; Sjöblom et al., 2008). The switch in equilibrium from actin stabilizers to actin modifiers generates a short time window that is triggered by NMDAR Ca^{2+} influx, in which the actin cytoskeleton becomes labile and susceptible to major reorganization. Thereafter, the stabilization of newly remodeled actin occurs by a steady increase of actin-stabilizing proteins in potentiated spines. In consequence, however, a stable pool of ABPs must exist for structural remodeling in the initial phase, helping to keep the elementary F-actin network in association

with the PSD (Bosch et al., 2014; Racz and Weinberg, 2004). Unfortunately, molecular machineries coupling local and rapid synaptic elevation of $[Ca^{2+}]_i$ to actin remodeling in the initial reorganization phase are currently unknown (Bosch et al., 2014; Kim et al., 2015; Okamoto et al., 2007).

In this study, we introduce a mechanism that can directly and instantaneously transduce local Ca^{2+}-signals to actin reorganization ensuring stabilization of the potentiated dendritic spines. In a series of *in vitro* and *in vivo* experiments, we show that elevations in $[Ca^{2+}]_i$ interrupt an intramolecular interaction in the postsynaptic Ca^{2+} sensor caldendrin that masks a series of PxxP motifs. Caldendrin then readily associates with the SH3 domain of the F-actin binding protein cortactin and releases the cortactin SH3 domain from back folding to its own proline-rich domain (PRD). This in turn protects F-actin against cofilin-induced severing, presumably at the base of spines, and promotes subsequent activation of the Arp2/3 complex via sequential recruitment of N-WASP. Genetic deletion or protein knockdown of caldendrin results in higher synaptic turnover of actin and cortactin, misarrangement of spinous F-actin nanostructure, loss of a stable synaptic F-actin pool, and impaired LTP and object recognition memory. These cellular and behavioral phenotypes can be rescued by application of the actin-stabilizing drug jasplaklinoide (JPK) or by re-expression of a wild type, but not a Ca^{2+}-binding mutant, of caldendrin in a null mutant background. Collectively the data show that Ca^{2+} binding to caldendrin following opening of NMDARs stabilizes a pool of F-actin that is required for structural remodeling of spines undergoing plasticity.

RESULTS

An Uncommon Mechanism for a Ca^{2+}-Dependent Target Interaction Allows for Binding of Caldendrin to the SH3 Domain of Cortactin

Caldendrin has a unique bipartite structure with a highly basic, proline- and arginine-rich N terminus and a calmodulin (CaM)-like, EF-hand-containing C terminus (Seidenbecher et al., 1998; Figure 1A). To learn more about a synaptic role of caldendrin, we reasoned that specific SH3-domain-containing binding partners for the N terminus might exist. We therefore probed SH3 domain protein arrays with a bacterially produced N-terminal fragment and found most prominent binding to the SH3 domain of cortactin (Figure 1B; Table S1). A caldendrin-specific antibody allowed the co-immuniprecipitation (co-IP) of cortactin from rat brain lysates, indicating that both proteins might be part of one complex *in vivo* (Figure 1C). Moreover, both proteins co-localize in dendritic spines of rat hippocampal primary neurons, as revealed by immunofluorescence staining, and both are also abundantly present in the PSD fraction (Figures S1A and S1B). Heterologous co-IP experiments independently confirmed an interaction of mCherry-cortactin with caldendrin-GFP in HEK293T cell lysates and showed that cortactin associates with the proline-rich N terminus of caldendrin, but not the EF-hand-containing C-terminal part (Figure 1D). Surprisingly, the interaction of full-length cortactin and caldendrin was much stronger in the presence of 0.5 mM Ca^{2+} than in Ca^{2+}-free conditions (Figure 1E). Subsequent GST-pull-down assays confirmed that bacterially expressed GST-cortactin also binds to untagged caldendrin from a HEK293T cell extract more efficiently in the presence of Ca^{2+}, whereas binding to the separated GFP-tagged N terminus in pull-down assays is not Ca^{2+}-sensitive (Figure 1F). A direct interaction was also confirmed when we performed the pull-down experiment with defined protein amounts of GST-cortactin and recombinant purified caldendrin in the presence of 10 μM Ca^{2+}, a free Ca^{2+} concentration that is readily observed in spine synapses (Figure 1G).

To narrow down the N-terminal binding region we then inserted point mutations and found that replacing two arginines at position 40 and 41 to alanine clearly reduced binding of caldendrin to cortactin (Figure S1C). To test further for a direct interaction and to analyze binding kinetics in more detail, we next used surface plasmon resonance (SPR). Immobilized SH3 domain of cortactin was probed for caldendrin interaction in the presence of either 0.5 mM Ca^{2+} or EGTA (Figures 1H and 1I). We found that caldendrin associates with the SH3 domain more readily in the presence of Ca^{2+} (Figures 1H and 1I) with an association rate constant (k_a) of 3.4×10^4 1/Ms and a global K_D of 0.4 μM (Figure 1J). Furthermore, the interaction is very stable with about 70% binding after 60 min in the presence of Ca^{2+} and 50% in the presence of EGTA, as judged by the dissociation kinetics (Figure 1H). A Ca^{2+}-binding mutant of caldendrin in which we replaced two aspartate residues (D243 and D280) in the Ca^{2+}-binding EF hands 3 and 4 with alanine (Figure S1D) showed much weaker binding affinity and a slower association rate, despite the presence of the PxxP motifs (K_D of 7.7 μM and a k_a of 1158 1/Ms) (Figure 1K). Comparable results were obtained with eukaryotically expressed proteins in heterologous co-immunoprecipitation experiments (Figure S1E). Finally, even higher association but comparable dissociation kinetics between full-length caldendrin and cortactin was measured in physiological Ca^{2+} concentrations (10 μM) in single-cycle titration mode SPR experiments (K_D of 0.42 μM and a k_a of 37.6×10^5 1/Ms) (Figure S1F). Thus, Ca^{2+} facilitates the association of caldendrin with the SH3 domain of cortactin and promotes stability of the complex.

Caldendrin Is a Fast Ca^{2+} Sensor and Ca^{2+} Binding Interrupts an Intramolcular Interaction in Caldendrin

These data make it likely that the accessibility of the N-terminal binding interface is regulated by a Ca^{2+}-dependent intramolecular interaction of caldendrin. Förster resonance energy transfer acceptor bleaching (FRET-AB) experiments performed in living COS-7 cells (Figures 2A and 2B) indeed revealed that YFP-caldendrin-CFP exhibited a robust FRET signal, while FRET efficiency was significantly reduced following bath application of the Ca^{2+} ionophore ionomycin (Figures 2A and 2B). In SPR experiments, we observed that the first 60 amino acids of the N terminus directly interact with the second EF-hand domain of caldendrin (Figure 2C; Table S2). Moreover, binding was much weaker in the presence of Ca^{2+} (Figure 2C; Table S2).

Taken together, these experiments suggest a unique mechanism of interaction that will likely not be competed by other EF-hand Ca^{2+}-sensors. However, the most closely related Ca^{2+} sensor, CaM, binds Ca^{2+} at a faster rate than even fast Ca^{2+} buffers (Faas et al., 2011); with respect to the abundance of

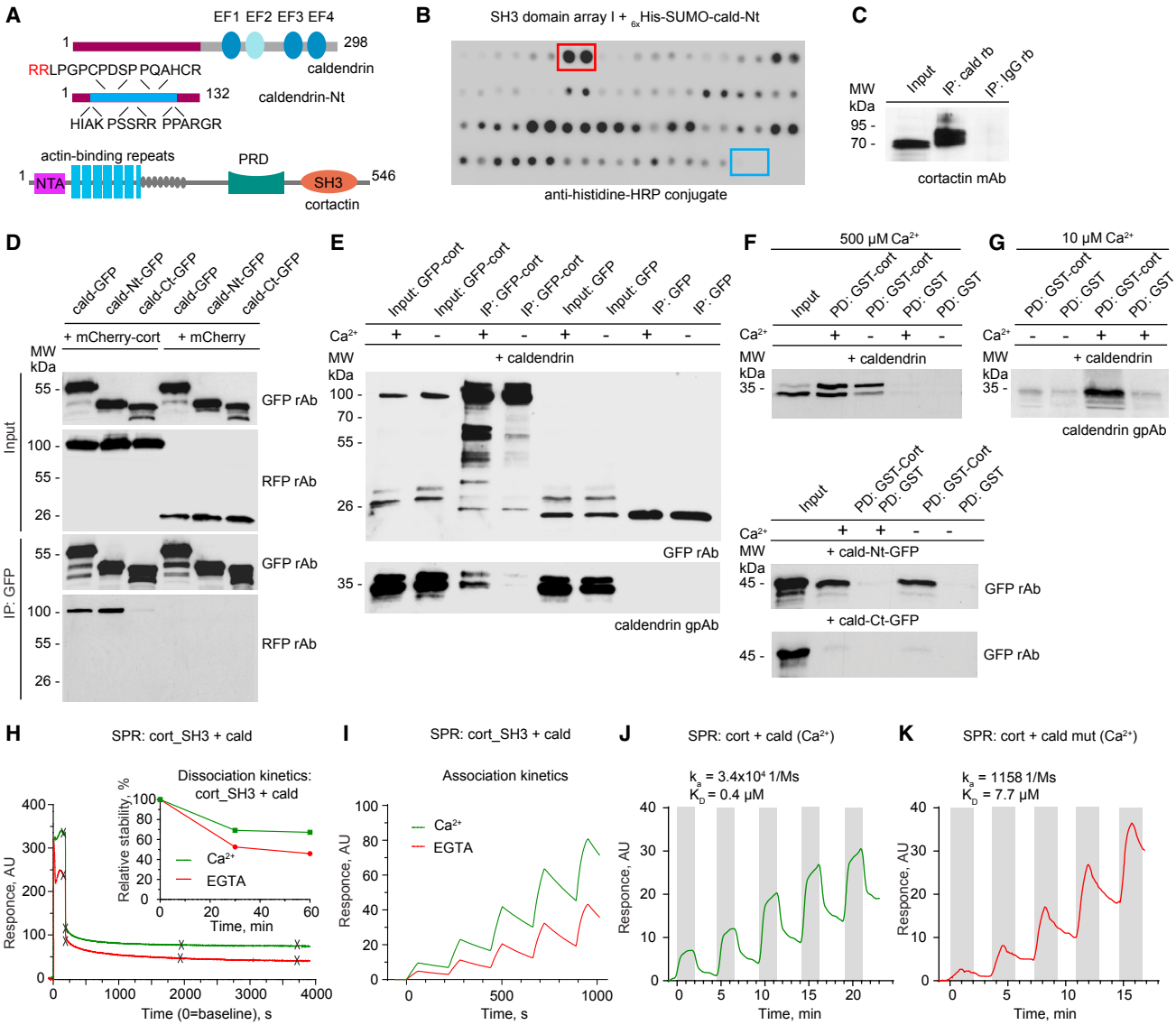

Figure 1. The Interaction of Caldendrin and Cortactin Is Modulated by Ca^{2+}

(A) Schematic representation of caldendrin and cortactin. NTA: N-terminal acidic domain; PRD: proline-rich domain. Light blue ellipse: cryptic EF hand; blue ellipse: functional EF hand. Critical arginines are highlighted in red.

(B) The interaction of the recombinant N terminus of caldendrin with different SH3-domains spotted on a SH3 domain array. Red box: cortactin; blue box: negative control. For array layout, see Table S1. 18 from the 38 SH domains probed belong to proteins with a synaptic localization.

(C) Co-IP of endogenous caldendrin and cortactin from an adult rat brain extract.

(D) Heterologous co-IP of full-length caldendrin-GFP and its C- and N-terminal truncation constructs with mCherry-cortactin expressed in HEK293T cells indicates that the interaction is mediated by the N terminus of caldendrin.

(E) Heterologous co-IP of cortactin-GFP and caldendrin expressed in HEK293T cells shows a Ca^{2+}-dependent interaction.

(F) Mapping of the binding region between caldendrin and cortactin by GST pull-down assays. The Ca^{2+} dependency is lost in separated N- or C-terminal protein fragments.

(G) Pull-down assay for purified GST-cortactin and untagged caldendrin shows the direct interaction of both proteins at physiological Ca^{2+} concentrations.

(H) SPR sensorgrams showing the interaction and stability of the complex formed by purified caldendrin and the SH3-domain of cortactin in absence and presence of Ca^{2+}. Note that the relative stability of the caldendrin-cortactin complex is higher in the presence of Ca^{2+}, as seen from the dissociation kinetics (inset).

(I) SPR sensorgrams of caldendrin injected over the immobilized SH3 domain of cortactin. Single-cycle kinetics measurements indicate a slower association rate in the absence of Ca^{2+}.

(J and K) SPR sensorgrams showing the interation between caldendrin (J) or its Ca^{2+} binding mutant (K) and full-length cortactin. Note a much higher association constant and affinity of the interaction of the wild-type protein. Caldendrin injection time is indicated in gray. See also Figures S1C and S1D.

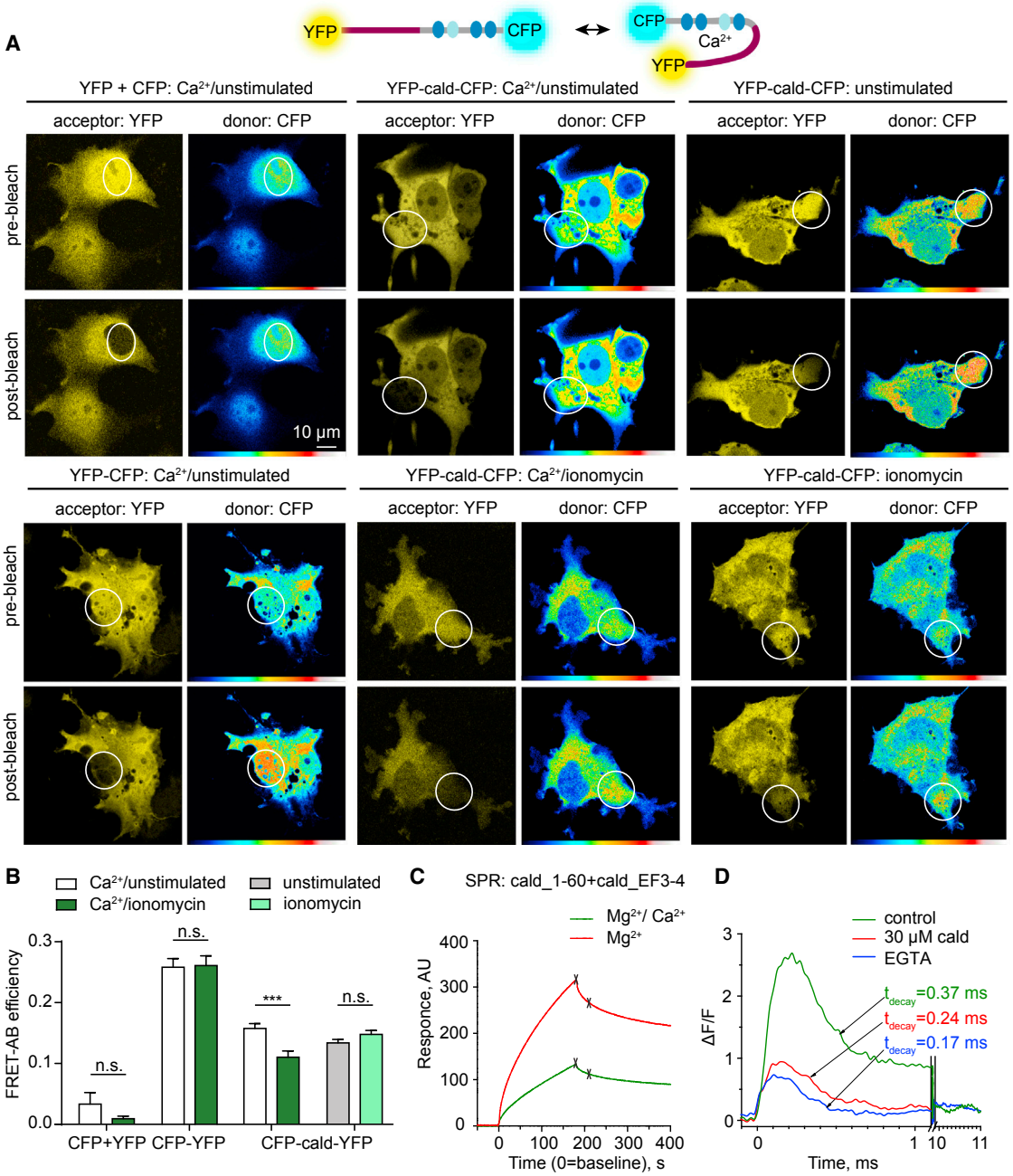

Figure 2. Caldendrin Exhibits Ca^{2+}-Dependent Back-Folding and Is a Fast Ca^{2+} Sensor

(A) FRET acceptor bleaching indicates Ca^{2+}-dependent back-folding of caldendrin. Representative images of COS-7 cells transfected with the indicated constructs before and after photo-bleaching of YFP. 2 µM of Ca^{2+}/ionomycin is used to increase intracellular Ca^{2+} levels. Stimulation with ionomycin in Ca^{2+}-free solution as control has no effect on caldendrin conformation. CFP fluorescence is shown in pseudocolors.

(B) Quantification of FRET efficiency in (A). Data are represented as mean ± SEM. n = 11 (CFP-YFP unstimulated and Ca^{2+}/ionomycin), n = 20 (YFP-cald-CFP unstimulated), n = 21 (YFP-cald-CFP Ca^{2+}/ionomycin), n = 10 for CFP and YFP (unstimulated and Ca^{2+}/ionomycin). n = number of cells. Unpaired, 2-tailed Student's t test, $^{**}p < 0.01$.

(C) SPR sensorgram demonstrating the interaction of the first 60 amino acids of caldendrin with the second EF-hand domain. The interaction is weaker upon Ca^{2+} binding. Maximum binding point and stability point are indicated. See also Table S2.

(D) Ca^{2+} binding kinetics of caldendrin measured by UV-induced release of Ca^{2+} from DM-Nitrophen. Decay time of OGB-5N fluorescence is indicated.

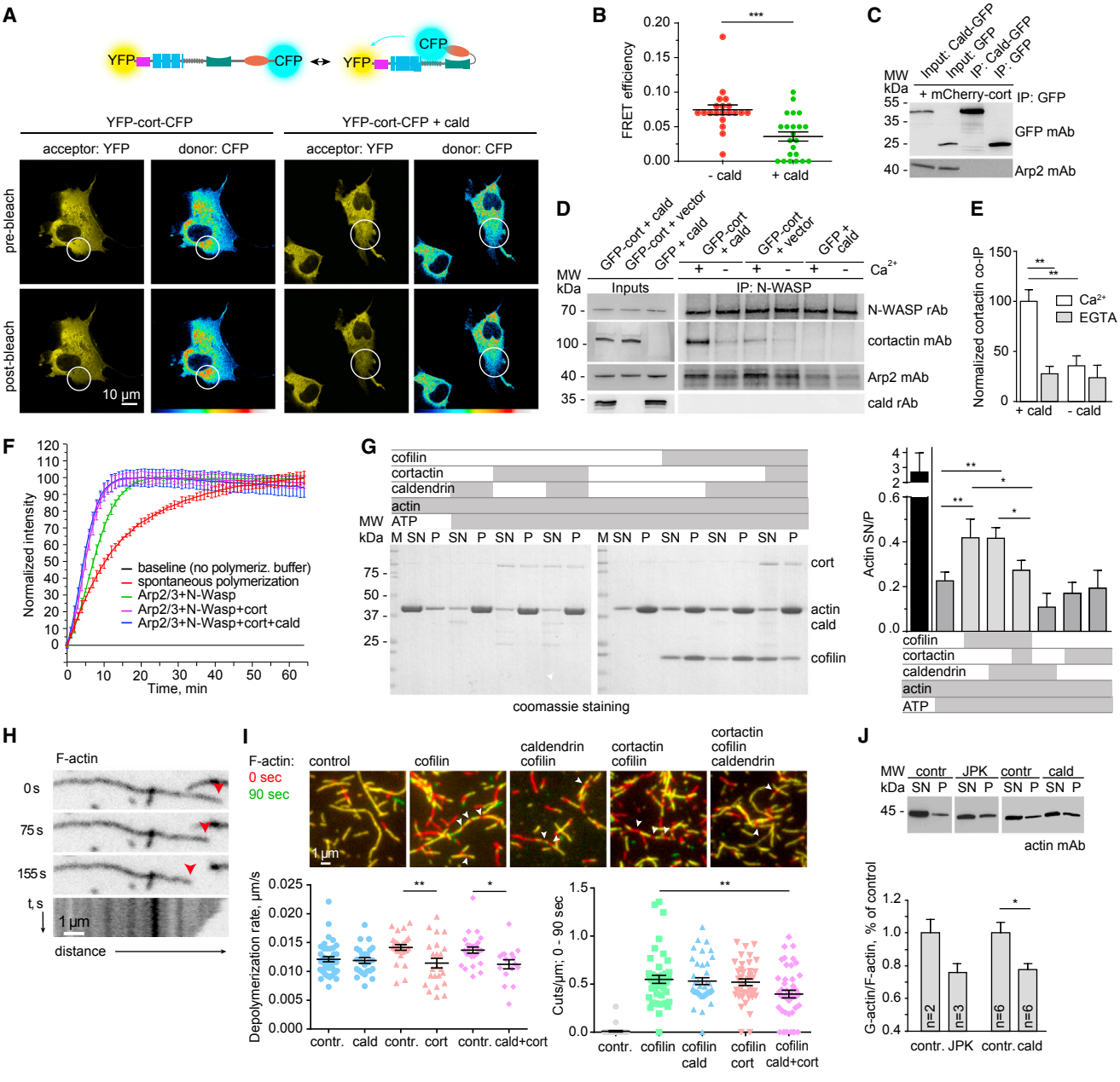

Figure 3. The Caldendrin-Cortactin Complex Promotes F-Actin Stability

(A) The back-folding of the SH3 domain of cortactin is competed by caldendrin. FRET AB of YFP-cortactin-CFP in live COS-7 cells. Representative images of COS-7 cells transfected with the indicated constructs before and after photo-bleaching of YFP. See also Figure S3A.

(B) Quantification of (A). Data are represented as mean ± SEM. Each dot represents an individual cell. Unpaired, 2-tailed Student's t test. ***$p < 0.001$.

(C) Co-IP with overexpressed caldendrin-GFP, mCherry-cortactin, and endogenous Arp2/3 from HEK293T cells. Arp2 is absent in the caldendrin complex.

(D and E) Heterologous co-IPs indicate an increased interaction between N-WASP and cortactin in the presence of Ca^{2+} and caldendrin. Note the absence of caldendrin in the N-WASP complex (D). Data are represented as mean ± SEM (E). n = 4 experimental replications, 2-way ANOVA with Tukey's post hoc test. **$p < 0.01$.

(F) Caldendrin has no effect on *in vitro* polymerization of pyrene-labeled actin measured by fluorometry. Data are represented as mean ± SEM. n = 3 experimental replications. See also Figures S3C and S3D.

(G) The caldendrin-cortactin complex attenuates F-actin severing activity of cofilin-1 in an *in vitro* actin depolymerization assay. Ratio of actin in supernatant (SN) and pellet fraction (P) in the indicated reactions is measured by SDS-PAGE. Data are represented as mean ± SEM. n = 4 experimental replications, 1-way ANOVA with Tukey's post hoc test. *$p < 0.05$, **$p < 0.01$.

(H) Spontaneous *in vitro* depolymerization of F-actin-Alexa Fluor 568 visualized by TIRF microscopy. Example of an actin filament undergoing depolymerization upon G-actin washout. Red arrowheads indicate the barbed ends of the filament.

(legend continued on next page)

CaM, the steep and short Ca^{2+} transients in spines, this fast association rate raises the question of whether caldendrin will be able to compete for Ca^{2+} binding with CaM, which is a prerequisite for a rapid Ca^{2+}-dependent target interaction (Raghuram et al., 2012). To address the kinetic properties of Ca^{2+} binding to caldendrin, we employed an ultrafast *in vitro* technique that has been previously used for measuring Ca^{2+}-binding properties of calbindin-D(28k) and CaM (Faas et al., 2011; Nägerl et al., 2000). The rapid increase in Ca^{2+} concentration following flash photolysis of Ca^{2+} caged with DM-Nitrophen (DM-N) can be detected with the fast fluorescent Ca^{2+} indicator Oregon Green 488 BAPTA-5N (OGB-5N) (Figures 2D and S2A–S2F). In the presence of caldendrin, the decay of the flash-induced fluorescence was reduced due to the Ca^{2+} binding by the protein and was similar to the kinetics of the Ca^{2+} chelator EGTA (control t_{decay} = 0.37 ms, caldendrin t_{decay} = 0.24 ms, EGTA t_{decay} = 0.17 ms) (Figure 2D). In a direct comparison, we found that at physiological concentrations of caldendrin (Figures S2G and S2H), the Ca^{2+} affinity of caldendrin is not distinguishable from those of CaM (Faas et al., 2011; Figurse S2E and S2F). Given that calcium binding kinetics of caldendrin are comparable with CaM, this indicates that the protein is able to rapidly sense Ca^{2+} transients in the range of 5–10 μM like they occur within the first milliseconds after the induction NMDAR-dependent LTP (Sabatini et al., 2002).

Caldendrin Binding Releases the Back-Folding of Cortactin and Promotes Cortactin-Mediated F-Actin Stabilization

Cortactin is a multidomain protein containing an N-terminal acidic region (NTA), which binds the Arp2/3 complex, actin-binding repeats that are important for association with F-actin, a PRD, and a C-terminal SH3 domain (Schnoor et al., 2018; Figure 1A). Self-inhibition by intramolecular interactions of the SH3 domain and PRD can be released either by phosphorylation or by competitive ligand binding to the SH3 domain (Schnoor et al., 2018; Martinez-Quiles et al., 2004). We found that COS-7 and HEK293T cells expressing caldendrin showed decreased FRET signals of a YFP-cortactin-CFP reporter measured in living cells and cell extracts, respectively (Figures 3A, 3B, and S3A). To confirm the interaction of active cortactin and caldendrin *in vivo*, we performed a replating assay with COS-7 cells double transfected with mCherry-cortactin and caldendrin-GFP. Under these conditions, active cortactin accumulates at motile lamelipodia containing branched F-actin, and caldendrin-GFP was enriched in the same locations (Figure S3B).

We next asked whether caldendrin binding impacts actin dynamics and first immunoprecipitated caldendrin-GFP/mCherry-cortactin from HEK293T cell lysates. We found that endogenous Arp2 is not present in this complex (Figure 3C). Cortactin weakly binds and activates the Arp2/3 complex on its own, but shows strong synergistic potentiation of actin polymerization, together with N-WASP, that also interacts with cortactin's SH3 domain. When we immunoprecipitated endogenous N-WASP from HEK293T cell lysates, we found Arp2 in the precipitate but did not find co-expressed untagged caldendrin (Figure 3D). Interestingly, in the presence of 0.5 mM Ca^{2+} and caldendrin, the band of cortactin in the N-WASP immunoprecipitate was much stronger (Figures 3D and 3E), suggesting a Ca^{2+}-dependent facilitating role of caldendrin for activation of cortactin and the subsequent association with the N-WASP-Arp2/3 complex.

To directly address the functional consequences of the interaction on actin dynamics, we performed a series of *in vitro* reconstitution assays. *In vitro* actin polymerization assays using recombinant proteins (Figure S3C) showed that addition of Arp2/3 complex and the VCA domain of WASP promoted *in vitro* polymerization of pyrene-labeled actin; this effect was futher enhanced by adding cortactin (Figures 3F and S3D). Of note, under these experimental conditions, the constitutively active VCA domain of WASP was used. This can bind Arp2/3 and actin monomers simultaneously and does not require active cortactin. The inclusion of caldendrin resulted in no further enhancement of actin polymerization (Figure 3F).

We therefore asked next whether the interaction with caldendrin might promote F-actin stability. *In vitro* depolymerization assay performed in the presence of cofilin revealed an increased amount of soluble actin versus filaments pelleted by ultracentrifugation (Figure 3G). Pre-incubation of actin filaments with purified caldendrin had no effect on cofilin-induced severing, but in the presence of both caldendrin and cortactin, cofilin severing was strongly reduced (Figure 3G). To discriminate spontaneous depolymerization from cofilin effects we employed TIRF microscopy. *In vitro* polymerization of Alexa-Fluor-568-conjugated actin occurs spontaneously at certain actin concentrations and reaches an equilibrium of G- and F-actin. We then added in different combinations of recombinant cofilin, cortactin, and caldendrin and determined the rate of F-actin depolymerization caused by G-actin wash-out and cofilin-severing efficiency by analyzing cuts in the filament (Figures 3H and 3I). The data showed a clear reduction of actin depolymerization in the presence of either cortactin or caldendrin-cortactin (Figure 3I). However, the number of cuts per μm of filament was only significantly reduced when both proteins were present (Figures 3I and S3E; Movie S1), indicating that the presence of caldendrin promotes F-actin stability by hindering cofilin severing. Furthermore, a G/F actin sedimentation assay in HEK293T cells revealed that caldendrin overexpression increased F-actin content to a similar extent as treatment with the actin stabilizer JPK (Figure 3J).

(I) Kymographs analysis of F-actin depolymerization rate indicates slower depolymerization in the presence of cortactin or caldendrin and cortactin together (lower left). Overlay images show the actin filaments before adding cofilin (green) and 100 s after (red) (top). Significant reduction in cofilin severing sites is seen in the presence of caldendrin and cortactin. Arrowheads are indicating cutting sites. Data are represented as mean ± SEM. Each dot represents an individual filament. Unpaired, 2-tailed Student's t test, *$p < 0.05$, **$p < 0.01$ (left), 1-way ANOVA with Bonferroni post hoc test. **$p < 0.01$ (right). See also Figure S3E and Movie S1.

(J) Immunoblot of actin and quantification of G/F actin ratio in an actin sedimentation assay showing that overexpression of caldendrin in COS-7 cells reduces the G/F actin ratio. Treatment with 1 μM of JPK is included as positive control. Data are represented as mean ± SEM. n = number of experimental replications. Unpaired, 2-tailed Student's t test. *$p < 0.05$.

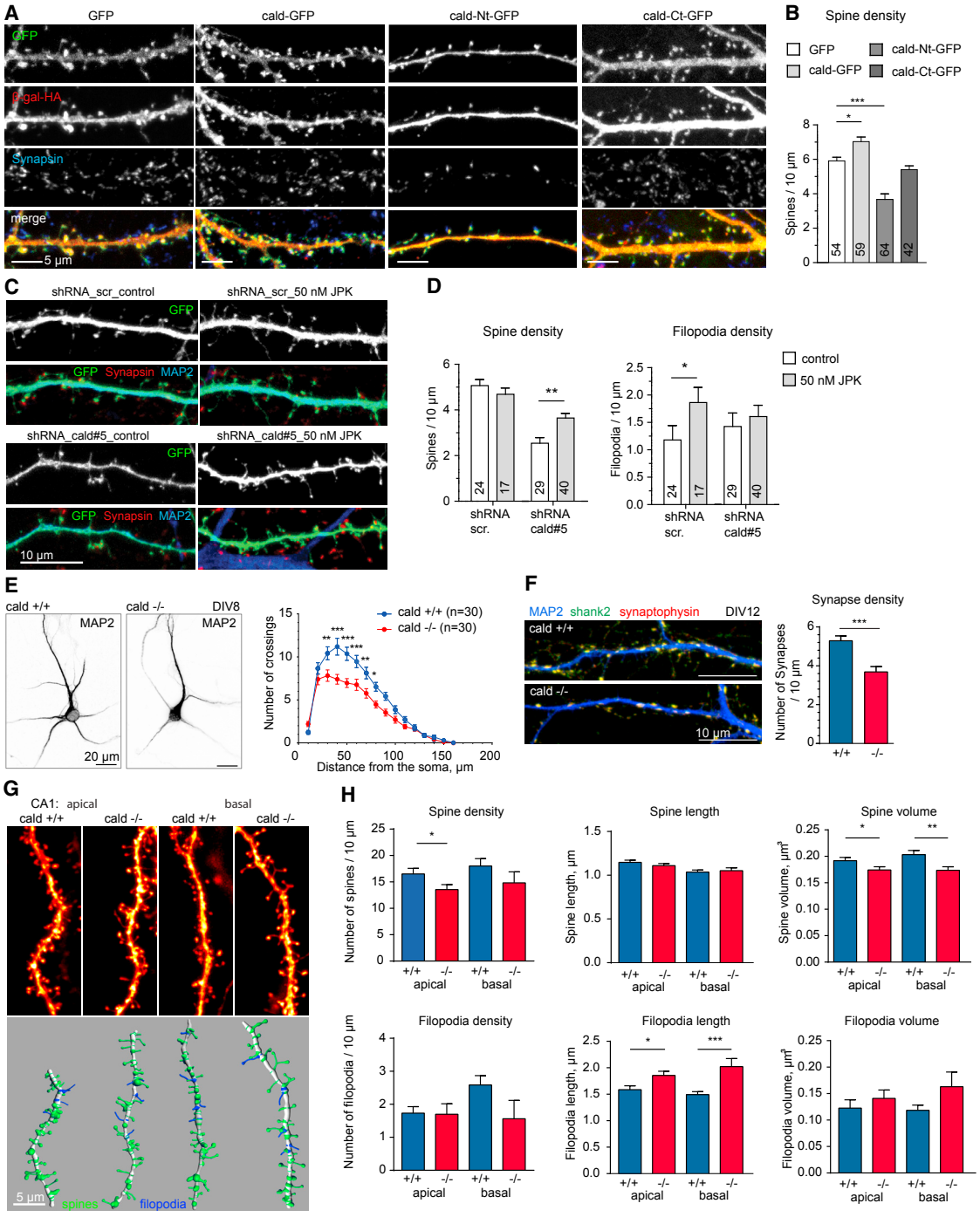

Figure 4. Effect of Caldendrin Overexpression and Deletion on Morphology of Dendritic Spines in Hippocampal Neurons

(A) Overexpression of caldendrin has positive effects on spine density, whereas overexpression of an N-terminal truncation construct or shRNA knockdown of caldendrin has the opposite effect. Representative maximum projections of confocal images of rat hippocampal primary neurons (DIV19) transfected with different GFP-tagged constructs of caldendrin and the volume marker beta-galactosidase are shown.

(B) Quantification of spine density from (A). Data are represented as mean ± SEM. n = number of dendritic segments. 1-way ANOVA with Bonferroni post hoc test. *$p < 0.05$, ***$p < 0.001$. See also Figure S4.

(C) Representative confocal images of dendritic segments from DIV16 primary hippocampal neurons transfected with shRNA directed against caldendrin or scrambled shRNA. The reduction of spine density upon caldendrin knockdown can be partially rescued by chronic application of 50 nM JPK. For further characterization, see Figure S4.

(legend continued on next page)

Caldendrin Deficiency Results in Simplification of Synapto-dendritic Cytoarchitecture

Cortactin plays a documented role in spine dynamics and dendrite development (Hering and Sheng, 2003; Chen and Hsueh, 2012). Similar to cortactin, caldendrin overexpression and shRNA knockdown had prominent effects on cell morphology of hippocampal primary neurons (Figures 4A–4D, S4A, and S4B). Caldendrin overexpression moderately increased the number of spines and the spine length of hippocampal primary neurons at day *in vitro* (DIV) 19 (Figures 4A, 4B, and S4A). Overexpression of the C-terminal EF-hand-containing part had no effect, while transfection of the N-terminal half even resulted in a reduction of spine number (Figures 4A and 4B). In addition, sholl analysis revealed a simplification of dendritic architecture when neurons were transfected at DIV9 with caldendrin shRNA (Figure S4C and S4D). At DIV14, when dendrites and synapses are already formed, caldendrin knockdown still induced a profound loss of spines (Figures 4C and 4D). This phenotype resembled those observed after shRNA knockdown of cortactin (Hering and Sheng, 2003), and it could be rescued by re-expression of shRNA-resistant caldendrin (Figures S4E–S4H) as well as by application of JPK (Figures 4C, 4D, S4C, and S4D).

To follow up on this finding, we next employed mouse hippocampal primary neurons derived from caldendrin-knockout mice (Figures S5A–S5C, 4E, and 4F). At DIV8, dendrites of *caldendrin*$^{-/-}$ neurons were less complex than those of wild-type neurons (Figure 4E), and the number of synapses at DIV12 was also significantly reduced (Figure 4F). This phenotype was milder in brain slices of *caldendrin*$^{-/-}$ mice (Figures 4G–4H and S5F–S5I). Of note, there was no change in cortactin expression in the brain of knockout mice (Figure S5D). Nissl stainings showed no major structural defects in the hippocampus of 12-week-old *caldendrin*$^{-/-}$ mice (Figure S5E). However, a closer inspection of CA1 neurons in hippocampal organotypic slices expressing mRuby2 revealed simplification of basal dendrites (Figures S5F–S5I), reduced spine number on apical dendrites, reduced spine size, and increased filopodia length (Figures 4G and 4H).

Caldendrin and Cortactin Are Required for BDNF-Induced Spine Size Potentiation

Activity-dependent actin remodeling is tightly controlled by a coordinated action of actin nucleation and severing as well as stabilization of the newly arranged actin cytoskeleton (Bosch et al., 2014; Noguchi et al., 2016). To test the role of caldendrin and cortactin on spine dynamics, we generated bicistronic lentiviral constructs expressing shRNA targeting caldendrin or cortactin and doxycyclin-inducible MARCKS-GFP as a membrane marker (Figures S6A and S6B). Virally delivered shRNA against caldendrin or cortactin induced a reduction in dendritic spine density at DIV19 and DIV27 (Figures S6C–S6E; Movie S2). We then induced synaptic plasticity by application of brain-derived neurotrophic factor (BDNF) (Iki et al., 2005; Molnár, 2011). Time-lapse imaging revealed that the fluctuation in total number of dendritic protrusions within 1 hr of BDNF application was clearly enhanced after knockdown of caldendrin or cortactin (Figures 5A and 5B; Movie S3). Longer treatment with BDNF (2 hr) resulted in induction of cLTP, as seen by increased surface staining of AMPA receptors (Figures S5J and S5K) and in an increase in number of dendritic spines (Figures 5C and 5D). Knockdown of both proteins prevented BDNF-induced spine growth as compared to cells infected with a control construct (Figures 5C, 5D, and S6F–S6H). In particular, the formation of new mushroom-like spines was abolished (Figure S6H). Collectively these data indicate that not actin polymerization but F-actin stability is controlled by the caldendrin-cortactin interaction.

Enhanced Synaptic Activity Triggers Conformational Change of Caldendrin and Increases the Association with Cortactin in Spines

The source of spinous calcium that will induce the open conformation in caldendrin is most likely calcium influx through synaptic NMDAR. We have, therefore, first assessed the NMDAR:AMPAR ratio in hippocampal CA1 neurons patched in the whole-cell mode in acute slices and found no difference between both genotypes (Figures S6I–S6K). We have also assessed mEPSC amplitude and frequency and found no difference between wild-type and *caldendrin*$^{-/-}$ neurons (Figures S6J and S6K). In the next series of experiments we asked whether caldendrin might associate with cortactin in spine synapses following the induction of plasticity. To this end, we transfected hippocampal primary neurons from *caldendrin*$^{-/-}$ mice with a CFP-caldendrin-YFP FRET construct. Cells were kept in silencing conditions (1 μM TTX) and then stimulated with the $GABA_A$ antagonist bicuculline, which rapidly enchances endogenous excitatory synaptic transmission and is used as an effective way to trigger synaptic plastcity in primary cultures (Figure S5J and S5K; Karpova et al., 2013). The population of

(D) Quantification of spine and filopodia density shown in (C). Data are represented as mean ± SEM. n = number of dendritic segments. 1-way ANOVA with Tukey's post hoc test, **p < 0.01 (spines), 2-way ANOVA with Bonferroni post hoc test.*p < 0.05 (filopodia).

(E) *Cald*$^{-/-}$ primary neurons show reduced dendritic arborization. Primary hippocampal cultures at DIV8 were stained for MAP2. Dendritic complexity was measured by sholl analysis. Data are represented as mean ± SEM. n = number of neurons. Repeated-measures-2-way ANOVA with Bonferroni post hoc test. *p < 0.05, **p < 0.01, ***p < 0.001.

(F) *Cald*$^{-/-}$ primary neurons at DIV12 show a reduced number of synaptic contacts visualized by double immunofluorescence stainings directed against shank2 and synaptophysin. Maximum projections of confocal images of dendritic branches are depicted. Data are represented as mean ± SEM. n numbers are n = 29 ($^{+/+}$), n = 30 ($^{-/-}$) dendritic segments. Unpaired, 2-tailed Student's t test, **p < 0.01.

(G) Maximum projections of confocal images of apical and basal dendritic segments of CA1 pyramidal neurons in organotypic hippocampal slices with corresponding 3D reconstructions.

(H) Quantification of protrusion densities and characteristics of (G). Data are represented as mean ± SEM. n numbers are for density measures—n = 16 (apical $^{-/-}$), n = 12 (apical $^{+/+}$), n = 7 (basal $^{-/-}$), n = 10 (basal $^{+/+}$) dendritic segments—and for characterization—n = 696 (apical $^{-/-}$), n = 577 (apical $^{+/+}$), n = 345 (basal $^{-/-}$), n = 543 (basal $^{+/+}$) protrusions. Unpaired, 2-tailed Student's t test, *p < 0.05, **p < 0.01, ***p < 0.001. See also Figure S5.

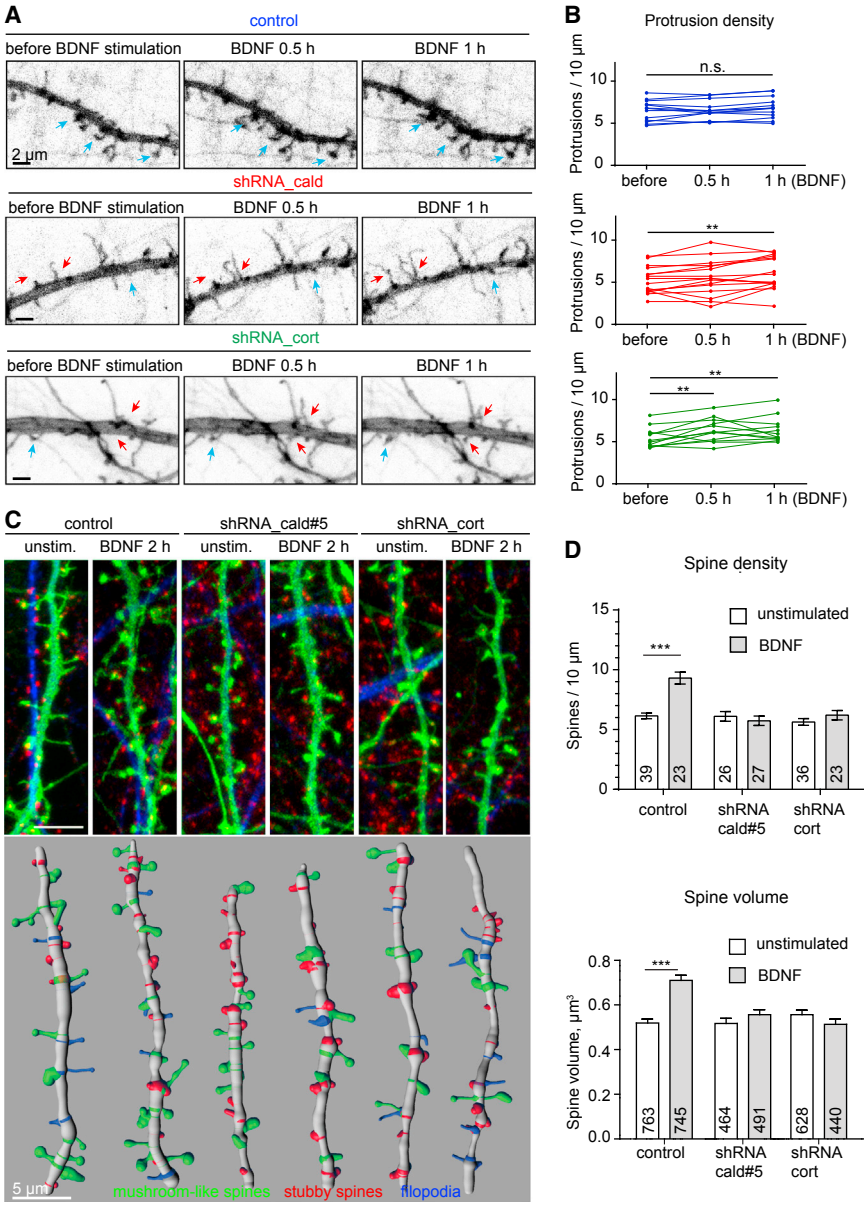

Figure 5. shRNA Knockdown of Caldendrin or Cortactin Abolishes BDNF-Induced Changes in Spine Density and Spine Size Potentiation

(A) Stills from time-lapse acquisitions from hippocampal primary neurons (DIV19) infected with indicated lentiviral constructs. Blue arrows show potentiated spines; red arrows show new appearing dendritic protrusions. See also Movie S3.

(B) Analysis of protrusion density from (A). n = number of neurons. Repeated-measures-2-way ANOVA with Tukey's post hoc test. $^{**}p < 0.01$.

(C) Analysis of BDNF-induced spine size potentiation in hippocampal primary neurons. Representative examples of maximum projection images from indicated groups and corresponding Imaris 3D reconstructions are depicted. Green: GFP; red: bassoon; blue: MAP2.

(D) Quantification of spine density and spine volume from (C). Data are represented as mean ± SEM. n numbers (neurons and spines, respectively) are indicated. 1-way ANOVA with Bonferroni post hoc test, $^{*}p < 0.05$. For further characterization, see Figures S5J and S5K and Figure S6.

spines showing FRET and the average FRET efficiency clearly declined after bicuculline treatment as compared to the measurement of the same neurons kept with TTX (Figures 6A and 6B), indicating a preferentially open conformation of caldendrin in activated synapses. Accordingly, we found a higher number of spines with stronger FRET signal between GFP-caldendrin-GFP and mCherry-cortactin under these conditions than in silenced controls (Figures 6C, 6D, and S6L). Thus, enhanced synaptic activity promotes the association of caldendrin and cortactin in spines.

Spinous F-Actin and Cortactin Dynamics Are Altered in Caldendrin-Deficient Neurons

In the next set of experiments we determined the turnover of actin and ABPs in spines of *caldendrin*$^{-/-}$ neurons. Mouse hippocampal primary neurons were co-transfected with GFP-actin and the volume marker mRuby2, and the fluorescence of both probes was monitored in individual spines at basal conditions (Figures S7A–S7C). The GFP-actin signal was highly correlated with those of mRuby2, indicating that GFP-actin can also be used to outline spine morphology (Figures S7A and S7B). We next monitored spinous GFP fluorescence over 5 min and found that it was much more variable, as evidenced by a higher standard deviation in *caldendrin*$^{-/-}$ neurons already under basal conditions (Figures 6E, 6F, and S7C).

The increased spine dynamics in *caldendrin*$^{-/-}$ neurons suggest a higher rate of actin polymerization and treadmilling, which results in shorter live times of actin filaments. F-actin in spines can be divided into a dynamic pool, with a turnover time below 1 min, and a stable F-actin pool, with a time constant of about 17 min (Koskinen and Hotulainen, 2014). About 81% of all spinous actin is in the filamentous form, of which most is present in a dynamic state and only 5%–15% is in a stable form (Honkura et al., 2008; Star et al., 2002). In support of the notion that the absence of caldendrin will increase spinous F-actin dynamics fluorescence, recovery was higher in *caldendrin*$^{-/-}$ neurons; this suggests a strong reduction in the size of the stable F-actin pool (mobile fraction: 68.2% ± 4.5% SEM and 93.5% ± 5% SEM after 1 min in $^{+/+}$ and $^{-/-}$ neurons, respectively) (Figures 6G and 6H). Enhanced synaptic activity following blockage of $GABA_A$ receptors with bicuculline increased the GFP-actin recovery rate in wild-type neurons but had no further effect in

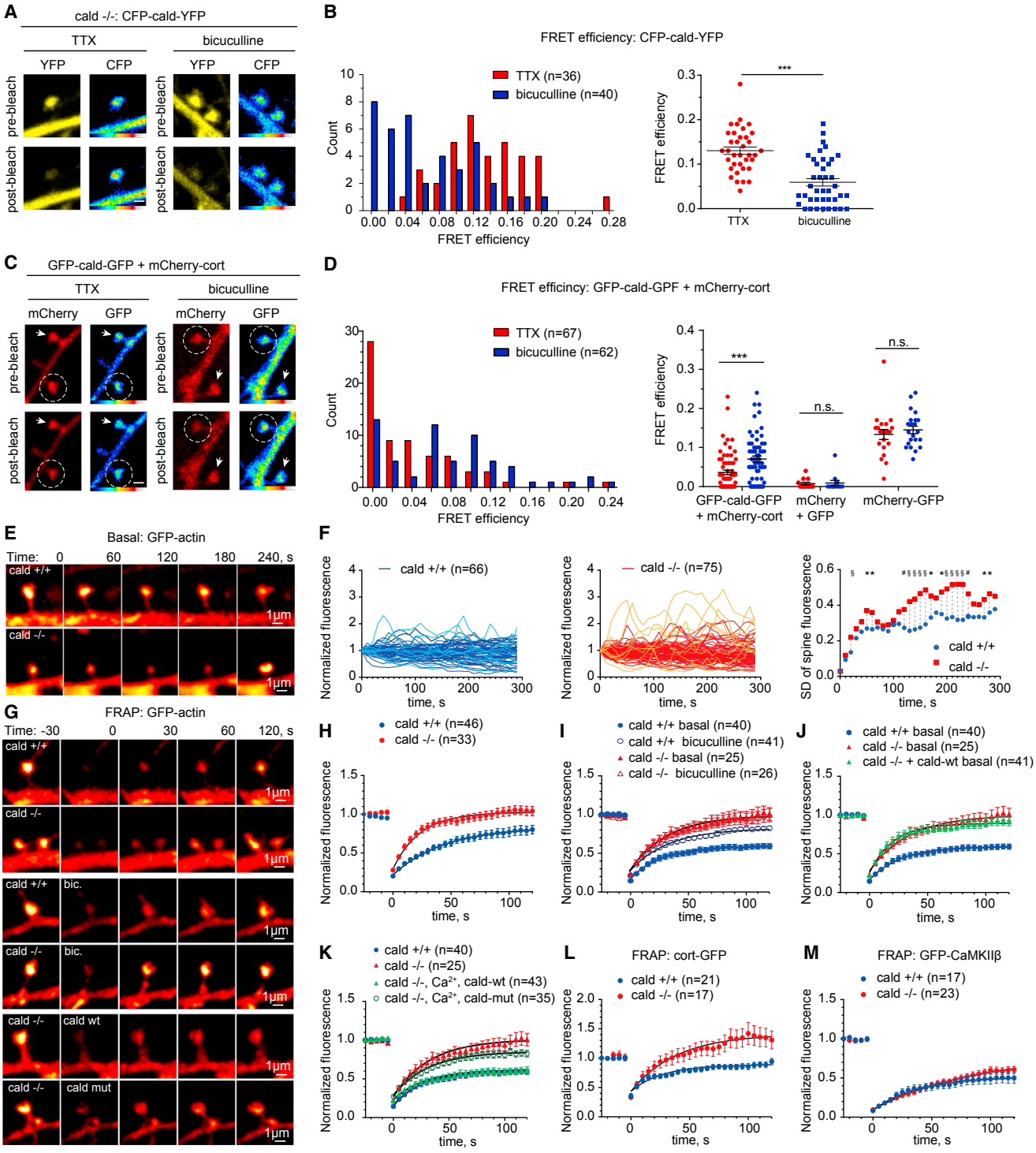

Figure 6. Caldendrin Regulates Actin and Cortactin Turnover in Spines

(A) Caldendrin changes its conformation upon bicuculline-induced synaptic activation. FRET acceptor bleaching (AB) in individual spines of *cald*$^{-/-}$ hippocampal primary cultures (DIV11/12) transfected with YFP-cald-CFP and silenced with TTX. FRET is measured in the presence of TTX and then after wash out and stimulation with bicuculline. Scale bar, 1 µm.

(B) Quantification of (A). Left: frequency distribution of FRET efficiencies in spines. Note increase in number of spines showing low FRET upon synaptic activation. Right: Mean FRET efficiency ± SEM. Unpaired, 2-tailed Student's t test. ***$p < 0.001$.

(legend continued on next page)

knockout cells (Figures 6G and 6I; Table S3). Most important, re-expression of wild-type caldendrin in *caldendrin*$^{-/-}$ neurons did not rescue the FRAP kinetics under resting conditions (Figures 6G and 6J; Table S3). A rescue was only seen when excitatory synaptic activity was enhanced with biccuculline prior to FRAP (Figures 6G and 6K; Table S3). These results suggest that synaptic caldendrin needs to first be loaded with Ca^{2+} to stabilize synaptic F-actin. Accordingly, the calcium-binding mutant of caldendrin could not rescue the FRAP phenotype even when synaptic activity was enhanced, indicating that Ca^{2+} binding is key for regulation of spinous actin dynamics (Figures 6G and 6K). Moreover, knockout neurons transfected with cortactin-GFP exhibited faster recovery after photobleaching than their wild-type counterparts, suggesting a weaker association of cortactin with the F-actin cytoskeleton in the absence of caldendrin (Figure 6L). In control experiments, FRAP of the unrelated F-actin binding protein, CaMKIIβ fused to GFP, was not altered in knockout neurons (Figure 6M). In conclusion, a stable synaptic pool of F-actin and cortactin is not detectable by FRAP in *caldendrin*$^{-/-}$ neurons.

The association of cortactin with dendritic spines is reportedly dynamic (Chen and Hsueh, 2012; Hering and Sheng, 2003; Iki et al., 2005; Seese et al., 2012). We indeed found that in rat and mouse hippocampal primary neurons, bicuculline stimulation resulted in a transient reduction of cortactin immunofluorescence at synaptic puncta within 5 min (Figures S7D–S7G). Hippocampal cultures prepared from *caldendrin*$^{-/-}$ mice exhibited a stronger reduction of synaptic cortactin immunofluorescence (Figures S7F and S7G), further suggesting that cortactin has a weaker association with spinous F-actin in the absence of caldendrin.

F-actin and ABPs are not uniformly distributed in the spine head but instead show specific enrichments in spinous nanocompartments (Chazeau et al., 2014; Racz and Weinberg, 2004, 2006). The major fraction of cortactin is associated with the spine core, where the stable pool of F-actin is localized (Racz and Weinberg, 2004). To address the question of how the nanostructure of the actin cytoskeleton is organized in *caldendrin*$^{-/-}$ neurons, we employed stimulated emission depletion (STED) nanoscopy of F-actin labeled with phalloidin-Atto647N. STED imaging revealed no genotype-dependent differences in organization of the cortical periodic F-actin lattice in axons, dendrites, and spine necks (Figure 7A). Actin filaments in mushroom-like spines of wild-type mice are frequently arranged in a cup-like shape outlining the membrane of the spine head (Figure 7B). In contrast, in neurons from *caldendrin*$^{-/-}$ mice, the filaments randomly filled the spine head (Figure 7B). The normalized phalloidin-Atto647N fluorescence intensity along the axis from the PSD to the spine neck was peaking near the base of the spine in wild-type neurons; it was more uniformly distributed over the spine head in *caldendrin*$^{-/-}$ neurons (Figures 7B and 7C), where F-actin peak intensity shifts toward the center of the spine (Figures 7D–7F). Thus, the lack of caldendrin induces a major topographical misarrangement in the nanoscale organization of the synaptic F-actin cytoskeleton (Figures 7B–7F). Along these lines, induction of structural LTP at individual spines in organotypic hippocampal slices with two-photon glutamate uncaging (Matsuzaki et al., 2004) results in a rapid increase in spine volume in both genotypes (Figures 7G and 7H). However, spine potentiation caused statistically significant large fluctuations in spine size only in *caldendrin*$^{-/-}$ neurons within the first 20 min (Figures 7G and 7I). These fluctuations were caused by repetitive expansion and shrinkage of the spine head, indicating aberrant F-actin remodeling during the early reorganization phase of structural spine plasticity (Figures 7H and 7I). Moreover, these differences cannot be explained by different calcium handling in both genotypes. When we performed calcium imaging in acute hippocampal slices, we found that following the induction of dendritic back-propagating action potentials spinous free $[Ca^{2+}_i]$ was not different in wild-type compared to knockout neurons (Figures S7H and S7I).

Deficits in LTP and Object Recognition Memory in *Caldendrin*$^{-/-}$ Mice Can Be Rescued by F-actin Stabilization with JPK

The experiments above indicate that the synaptic phenotype in caldendrin-knockout mice is related to reduced F-actin stability, increased actin turnover, and misarrangement of sub-spinous F-actin nanodomains. Next, to test the physiological properties of such synapses, we performed a series of experiments in acute

(C) FRET AB in individual spines of hippocampal primary cultures (DIV14-17) transfected with indicated constructs upon silencing with TTX and stimulation with bicuculline. Circle indicates spine with photo-bleached mCherry; the white arrow points to control spine. Note the increase in interaction of caldendrin and cortactin upon synaptic stimulation. Scale bar, 1 μm.
(D) Quantification of (C). Left: frequency distribution of FRET efficiencies in spines. Note increase in number of spines showing higher FRET upon synaptic activation. Right: Mean FRET efficiency ± SEM. Unpaired, 2-tailed Student's t test. ***$p < 0.001$.
(E) Individual frames from time-lapse imaging of GFP-actin in *cald*$^{+/+}$ and $^{-/-}$ primary hippocampal neurons.
(F) Normalized individual traces of GFP-actin level in analyzed spines (In E, different colors are use to highlight some of the traces) and standard deviations of mean GFP-actin intensities show higher fluctuations of spinous actin in *cald*$^{-/-}$. F test to compare variances. *$p < 0.05$, #$p < 0.01$, $$p < 0.001$.
(G) Stills from FRAP experiments in DIV9-12 mouse hippocampal neurons transfected with GFP-actin. Numbers indicate time relative to bleaching time, t = 0.
(H) Quantification of GFP-actin FRAP data (shown in G, upper) shows much faster recovery of GFP-actin in *cald*$^{-/-}$.
(I) Quantification of GFP-actin FRAP data upon bicuculline stimulation (G, middle) demonstrates a facilitated recovery rate in *cald*$^{+/+}$ but not in *cald*$^{-/-}$ neurons.
(J) Quantification of GFP-actin FRAP (G, middle and lower) shows no rescue after re-introducing caldendrin to *cald*$^{-/-}$ neurons under basal conditions. FRAP data for the basal conditions are the same as in (H).
(K) Analysis of the recovery time for GFP-actin in *cald*$^{+/+}$ and $^{-/-}$ neurons after overexpression of the wild-type and Ca^{2+}-binding mutant of caldendrin. Pre-loading of neurons with Ca^{2+} by 5 min bicuculline stimulation 8 hr prior to the experiment rescued the stable actin pool only upon expression of the caldendrin wild-type, but not the Ca^{2+} binding mutant protein. FRAP data for the basal conditions are the same as in (H).
(L and M) *Cald*$^{-/-}$ neurons show faster recovery of synaptic GFP-cortactin (L) in FRAP experiments but do not differ in recovery time of GFP-CaMKIIβ (M).
See also Table S3. Indicated n numbers are numbers of spines throughout the figure.

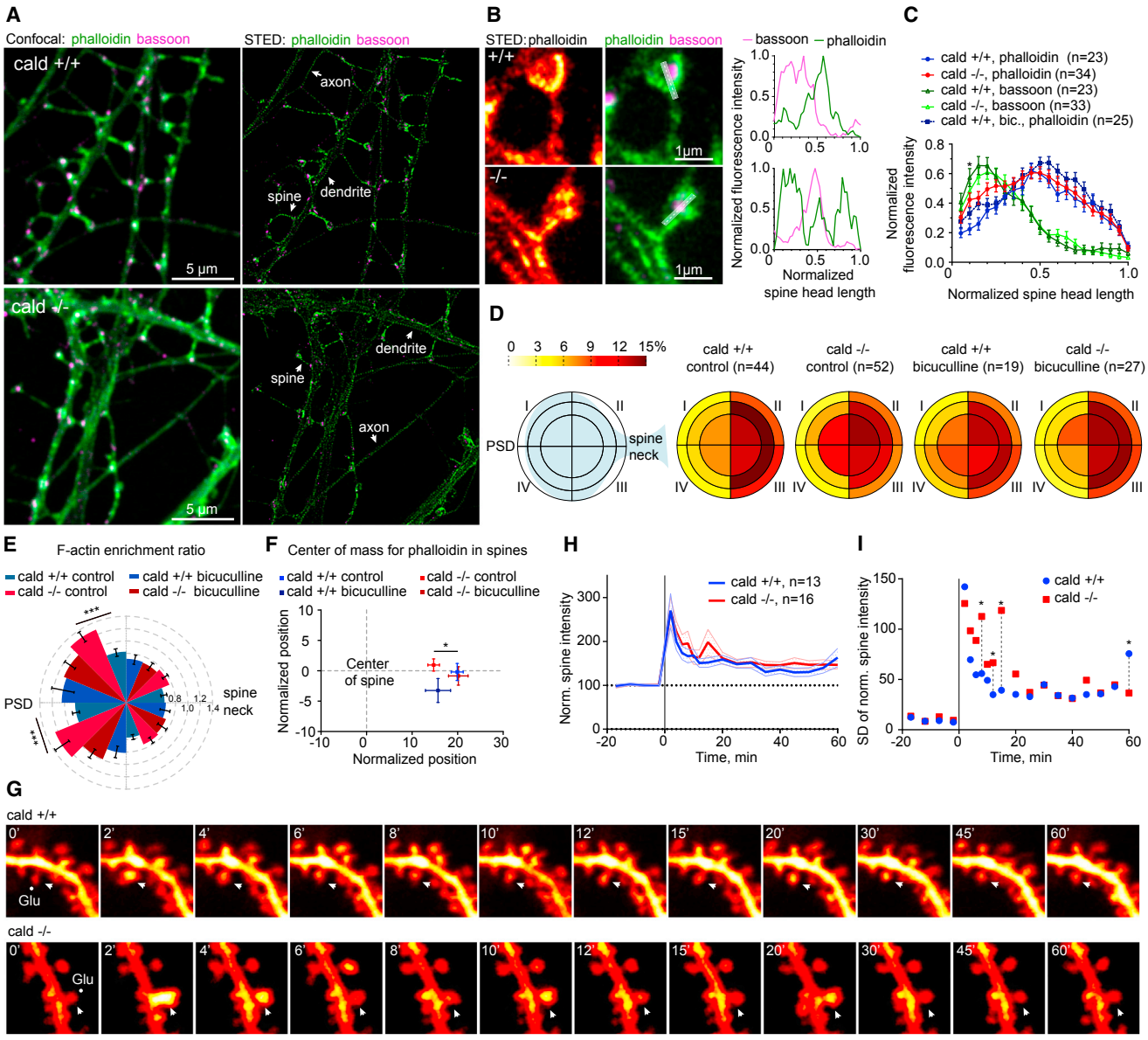

Figure 7. Lack of Caldendrin Causes Misarrangement of Spinous F-Actin at the Nanoscale Level

(A) Confocal and STED images of *cald*$^{+/+}$ and $^{-/-}$ hippocampal primary neurons (DIV18) stained with phalloidin-Atto647N, bassoon, and MAP2 antibody show no defects in periodic organization of cortical actin cytoskeleton. White arrows indicate actin rings in axons, dendrites, and spine neck.

(B and C) STED nanoscopy (B) reveals disordered spinous F-actin organization in *cald*$^{-/-}$ in comparison to cup-like actin enrichment in *cald*$^{+/+}$ (left). Right: example line scans from PSD to spine neck and mean values (C) indicate more diffuse distribution of F-actin in *cald*$^{-/-}$ spines. Data are represented as mean ± SEM. 2-way ANOVA with Sidak's post hoc test. *p < 0.05 ($^{+/+}$ versus $^{-/-}$).

(D) Analysis of subspinous distribution of F-actin in mushroom-like spines. Schematic explaining the sector analysis and mean values for individual sectors in indicated genotypes and conditions. Note the higher F-actin fluorescence intensity in the center of the spine in *cald*$^{-/-}$ neurons (inner segments of quadrants I and IV).

(E and F) Actin enrichment ratio (inner versus middle plus outer) for each quadrant shows significant shift in F-actin distribution from spine periphery to center in *cald*$^{-/-}$ (E). Data are represented as mean ± SEM. n numbers are n = 44 ($^{+/+}$ control), n = 52 ($^{-/-}$ control), n = 19 ($^{+/+}$ bicuculline), and n = 27 ($^{-/-}$ bicuculline). 2-way ANOVA with Tukey's post hoc test, ***p < 0.001. This is confirmed by a shift of position of the relative center of mass (F). Data are represented as mean ± SEM. 1-way ANOVA with Bonferroni post hoc test, *p < 0.05 ($^{+/+}$ control versus $^{-/-}$ control).

(G and H) Individual frames from time-lapse imaging of CA1 neurons transfected with eYFP following 2-photon glutamate uncaging in organotypic hippocampal mouse slices (G). Note strong fluctuations in spine size within the first 20 min after potentiation in *cald*$^{-/-}$ neurons. *Cald*$^{+/+}$ spines show expected rapid spine size increase directly after uncaging, which gradually decreases to 150% potentiation after 1 hr (H). Dot indicates point of glutamate uncaging; white arrows indicate potentiated spine.

(I) Higher standard deviation values are seen in *caldendrin*$^{-/-}$ spines within first 20 min after spine potentiation. F-test to compare variance of spine size between *cald*$^{+/+}$ and $^{-/-}$. *p < 0.05. Slices from 6 *cald*$^{+/+}$ and 5 *cald*$^{-/-}$ mice were used.

Indicated n numbers are numbers of spines throughout the figure.

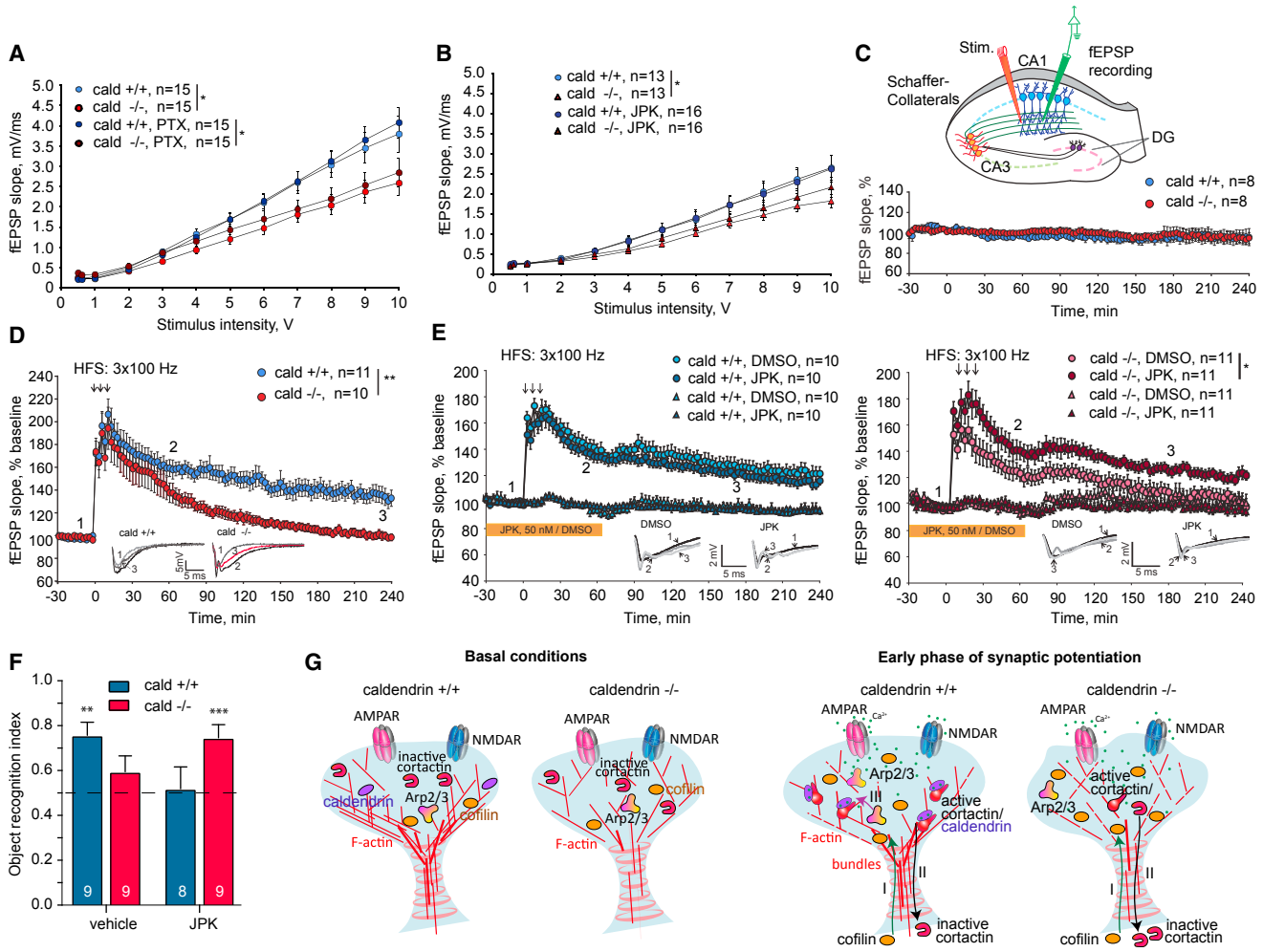

Figure 8. Caldendrin-Knockout Mice Show Severely Diminished CA1 LTP and Impaired Performance in Hippocampus-Specific Memory Task due to Impaired Activity-Dependent Spine Stabilization

(A and B) Input/output (I/O) curves show reduced synaptic strength in *cald*$^{-/-}$ mice. PTX, picrotoxin (A); JPK, jasplakinolide (B). n = number of slices from 4 to 5 animals per genotype and group. 2-way ANOVA, *p < 0.05.

(C) Stable baseline recordings of fEPSPs in *cald*$^{+/+}$ and *cald*$^{-/-}$. Stim.: stimulation electrode; n = number of slices; 1 slice per animal.

(D) *Cald*$^{-/-}$ mice show impaired HFS CA1-LTP maintenance in acute hippocampal slices compared to wild-type littermates. Inlets show representative fEPSPs traces at indicated time points: 1 = baseline, 2 = early LTP, 3 = late LTP. n = number of slices; 1 slice per animal. 2-way ANOVA, **p < 0.01.

(E) Application of 50 nM JPK during LTP induction rescues LTP phenotype in *cald*$^{-/-}$ mice, while it has no effect on LTP in wild-type mice. Inlets as in (D). All data are represented as mean ± SEM. n = number of slices; 1 slice per animal. 2-way ANOVA, *p < 0.05.

(F) Deficit in object recognition memory in *cald*$^{-/-}$ mice and its rescue upon intra-hippocampal application of JPK. On left, experimental protocol for analyzing the effect of JPK on novel memory recognition task. On right, data (mean ± SEM) show the preference for investigation of a novel object, tested 2 hr after memory acquisition. n = number of animals. 1-sample t test against chance (0.5), **p < 0.01, ***p < 0.001.

(G) Model depicting the role of caldendrin and cortactin during the initial phase of synaptic potentiation. Ca^{2+} increase upon synaptic stimulation is rapidly intercepted by caldendrin, which then can bind and activate cortactin via a conformational change. This complex exists over extended periods of time and can bridge the initial calcium influx with the later changes in molecular composition of the spine, resulting in stabilization of synapses. Active and caldendrin-bound cortactin is anchored to F-actin during the fast reorganization of synaptic molecules characteristic for early LTP. I: synaptic cofilin increase following NMDAR activation. Cofilin severs F-actin, thus allowing generation of new filaments and reorganization of the spine. II: At the same time, inactive cortactin leaves the spine. A minimal number of actin filaments are protected from severing by caldendrin-cortactin complex. *Cald*$^{-/-}$ mice show much higher F-actin turnover and loss of synaptic cortactin upon stimulation. Several minutes after the initial potentiation phase, F-actin branches are stabilized by caldendrin-cortactin complex. In addition, caldendrin could dissociate from cortactin in the vicinity of the PSD and allow binding of the Arp2/3 complex via N-WASP, allowing further Arp2/3-dependent polymerization (III).

hippocampal slices. The input-out (I/O) curve for the fEPSP slope was reduced (Figure 8A) in *caldendrin*$^{-/-}$ mice, while paired-pulse facilitation was normal (Figure S8A), pointing to a postsynaptic defect. In addition, treatment of the slices with JPK partially rescued the shift in the I/O curve (Figure 8B). Since the synaptic phenotype in caldendrin-knockout mice indicates the absence

of a stable F-actin pool in the intial reorganization phase of LTP, it is not surprising that Schaffer collateral late LTP (> 120 min following tetanization) was almost absent in slices from knockout mice, while the induction of LTP was identical in both genotypes (Figures 8C and 8D). Interestingly, bath perfusion of JPK at concentrations that had no effect on the induction and maintenance of LTP in hippocampal slices from wild-type mice clearly attenuated the impairment in late LTP in slices from knockout mice (Figure 8E).

Object recognition memory is sensitive to interruption of NMDAR-dependent LTP at hippocampal CA1 synapses (Clarke et al., 2010). We indeed found correspondence to the LTP phenotype impairments in object recognition in *caldendrin*$^{-/-}$ mice (Figure 8F). In control experiments, open-field and anxiety-related behavior in the elevated plus maze was normal, pointing to a cognitive deficit (Figure S8D). This deficit could be partially rescued by intrahippocampal infusion of JPK into the dorsal CA1 at a concentration that negatively impacts memory formation in wild-type mice (Figures 8F and S8B). Thus, stabilizing F-actin is even beneficial at the behavioral level, and it improves cognition, which underscores that a major spine function of caldendrin is indeed related to actin remodeling.

DISCUSSION

In this study, we report with a series of *in vitro* and *in vivo* experiments an unexpected role of a neuronal Ca^{2+}-binding protein in stabilization of actin filaments. We show that caldendrin is a fast Ca^{2+} sensor, able to compete with CaM by synaptic abundance and ''on'' rate of Ca^{2+} filling. Ca^{2+} binding results in unfolding of caldendrin, exposure of an N-terminal proline-rich region, and rapid association with the SH3-domain of cortactin. In molecular terms, caldendrin binding keeps cortactin in an active, open conformation, which promotes a sustained association with F-actin and specifically prevents cofilin-mediated filament severing (Figure 8G). Most likely, caldendrin-cortactin decorate the F-actin filaments and provide steric hindrance against cofilin-induced severing. Moreover, the prevailing association of cortactin with branch points of actin filaments (Helgeson and Nolen, 2013) suggests that caldendrin-cortactin will protect a minimal pool of branched actin. In mature spines of hippocampal neurons, cofilin avoids the spine core and instead concentrates in the spine head periphery and within the postsynaptic density (Racz and Weinberg, 2006). Translated into a cellular context, the data therefore suggest a scenario in which spinous Ca^{2+} transients target caldendrin-cortactin to F-actin located in two spatially segregated sub-compartments. Following the initial phase of Ca^{2+} influx, a long-lasting association of caldendrin and cortactin protects a stable pool of actin filaments, aligning the spine head membrane near the base of the spine. Indeed, immunogold labeling combined with electron microscopy demonstrated that cortactin concentrates within the spine base, and only a small fraction is adjacent to the PSD (Racz and Weinberg, 2004). We propose that, near the PSD, a more transient interaction—where caldendrin is subsequently replaced by membrane-bound N-WASP—might occur and will allow for facilitated actin polymerization. This model is supported by the fact that branched F-actin nucleation machineries like Arp2/3 complexes surround the PSD (Chazeau et al., 2014).

The initial spatio-temporal control of F-actin dynamics by caldendrin-cortactin is essential for the stabilization of LTP. Our data suggest that activity-dependent remodeling of the actin cytoskeleton requires, in the early phase, a minimal remaining cytoskeletal structure. Relatively little is known about the initial phase of F-actin remodeling in response to elevated $[Ca^{2+}]_i$ following NMDAR stimulation. Although numerous signaling pathways downstream of NMDAR-activation have been identified (Okamoto et al., 2009), the molecular mechanisms controlling actual remodeling of the spine are still largely elusive. Previous work suggests that cofilin shows a rapid accumulation in spines undergoing early LTP (Bosch et al., 2014). Severing of F-actin is essential for generation of barbed ends, which serve as F-actin nucleation points. Subsequent spine entry of other ABPs increases stability of newly formed filaments and eventually leads to reorganization of the PSD (Bosch et al., 2014; Chazeau et al., 2014). Caldendrin retains cortactin in an open conformation and promotes F-actin stability and subsequent polymerization (Figure 8G), and the fast Ca^{2+}-dependent association rate of the caldendrin-cortactin complex places the protein in a central position to bridge early with late-phase LTP. Taken together, the data show a direct mechanistic link between initial Ca^{2+}-induced actin re-organization in dendritic spines and long-term effects on spine potentiation and stability.

Along these lines, we found deficits in object recognition memory in *caldendrin*$^{-/-}$ mice that we could, at least in part, rescue by infusion of JPK into the dorsal CA1 region of the hippocampus at a concentration that has detrimental effects in wild-type mice. This result most likely reflects differences in spinous F-actin stability in wild-type and knockout mice. In wild-type mice, JPK will induce a shift toward highly stable F-actin, which is detrimental for actin-dependent reorganization of the PSD, potentially by reduced *de novo* F-actin branching following the induction of LTP. In knockout mice, however, JPK will promote a minimal stable pool of F-actin that is important for subsequent reorganization of the spine cytoskeleton.

It is quite striking that caldendrin plays a role in this very early step of F-actin remodeling (Figure 8G), which is in several aspects opposite to the role recently decribed for CaMKIIβ (Kim et al., 2015; Okamoto et al., 2009). Inactive CaMKIIβ binds to actin filaments and inhibits the interaction of other ABPs with F-actin. Activation by Ca^{2+}-CaM and subsequent autophosphorylation of the F-actin binding domain then interrupts F-actin binding and allows for the association with proteins involved in actin remodeling. Caldendrin-cortactin is probably part of a counteracting system that, by sensing the same Ca^{2+} signal, will stabilize F-actin. It is tempting to speculate that in both cases the directionality and kinetics of the spinous Ca^{2+} transient will have impact on the F-actin structures that are stabilized or depolymerized.

Finally, exposure of a proline-rich binding interface in response to EF-hand Ca^{2+} binding is an uncommon mechanism for a Ca^{2+}-regulated target interaction that is probably unique to caldendrin (Figures 1A and 8G). Thus, it is likely that cortactin activation is a caldendrin-specific and CaM-independent

function, and probably no other neuronal EF-hand calcium sensor will be able compensate for this role. A lack of compensation can explain the strong F-actin-related structural and functional phenotypes in spines following caldendrin protein knockdown and gene knockout, which are unexpected for an EF-hand CaM-like Ca^{2+}-sensor protein.

STAR★METHODS

Detailed methods are provided in the online version of this paper and include the following:

- KEY RESOURCES TABLE
- CONTACT FOR REAGENT AND RESOURCE SHARING
- EXPERIMENTAL MODEL AND SUBJECT DETAILS
  - Animals
  - Generation of caldendrin-knockout mice
  - Cell culturing conditions
- METHOD DETAILS
  - Antibodies
  - Biochemistry
  - Biophysics
  - *In vitro* actin assays
  - Cell culture and microscopy
  - Immunocytochemistry
  - Microscopy
  - Glutamate uncaging experiments
  - Electrophysiology in acute hippocampal slices
  - Behavior
- QUANTIFICATION AND STATISTICAL ANALYSIS
  - Analysis of dendritic morphology
  - 3D reconstructions and spine analysis in Imaris
  - Quantification of synaptic puncta
  - Analysis of actin distribution in spine heads
  - Statistical analysis
- DATA AND SOFTWARE AVAILABILITY

SUPPLEMENTAL INFORMATION

Supplemental Information includes eight figures, three tables, and three movies and can be found with this article online at https://doi.org/10.1016/j.neuron.2018.01.046.

ACKNOWLEDGMENTS

We are thankful to C. Borutzki, M. Marunde, S. Hochmuth, and S. Wehrmann for excellent technical support and B. Cloin for help with data analysis. We thank UMIF for providing access to confocal microscopes. This work was supported by grants from the European Molecular Biology Organization (EMBO) Long-Term Fellowship (EMBO ALTF 884-2011), the Deutsche Forschungsgemeinschaft (DFG) Emmy-Noether Programm (MI 1923/1-1), FOR2419 (MI 1923/2-1) to M.M., and DFG MI1923/3-1 to M.M., E.Y.L., and M.R.K. Support for M.R.K is by grants from the DFG (Kr1879 3-1,Kr18795-1, Kr18796-1, and SFB 779 TPB8), the Bundesministerium für Bildung und Forschung 'Energi' FKZ: 01GQ1421B, The EU Joint Programme – Neurodegenerative Disease Research (JPND) project STAD, People Programme (Marie Curie Actions) of the European Union's Seventh Framework Programme FP7/2007-2013/ under REA grant agreement n° [289581], and the Leibniz Foundation (Pakt für Forschung 2014, 2015, 2017). C.C.H. was supported by the Netherlands Organisation for Scientific Research (NWO; NWO-ALW-VICI) and the European Research Council (ERC consolidator, 617050, NeuroMT). P.S. was supported by the Swiss National Science Foundation (PBZHP3-147307). E.Y.L. was supported by the Russian Foundation for Basic Research (16-58-12017).

AUTHOR CONTRIBUTIONS

M.M., C.C.H., and M.R.K. designed the study. M.M., J.B., P.S., B.v.B., P.Y., J.H., P.P.R., A.K., E.Y.L., R.R., J.L.-R., C.S., and S.A.R. conducted the experiments. M.M., J.B., B.v.B., P.S., P.Y., J.H., A.K., E.Y.L., J.L.-R., O.K., S.A.R., O.S., and M.R.K. analyzed data. M.M. and M.R.K. wrote the paper, and all authors commented on and revised the manuscript.

DECLARATION OF INTERESTS

The authors declare no competing interests.

Received: July 14, 2017
Revised: December 18, 2017
Accepted: January 26, 2018
Published: February 22, 2018

REFERENCES

Albrecht, A., Çalışkan, G., Oitzl, M.S., Heinemann, U., and Stork, O. (2013). Long-lasting increase of corticosterone after fear memory reactivation: anxiolytic effects and network activity modulation in the ventral hippocampus. Neuropsychopharmacology *38*, 386–394.

Bosch, M., and Hayashi, Y. (2012). Structural plasticity of dendritic spines. Curr. Opin. Neurobiol. *22*, 383–388.

Bosch, M., Castro, J., Saneyoshi, T., Matsuno, H., Sur, M., and Hayashi, Y. (2014). Structural and molecular remodeling of dendritic spine substructures during long-term potentiation. Neuron *82*, 444–459.

Chazeau, A., Mehidi, A., Nair, D., Gautier, J.J., Leduc, C., Chamma, I., Kage, F., Kechkar, A., Thoumine, O., Rottner, K., et al. (2014). Nanoscale segregation of actin nucleation and elongation factors determines dendritic spine protrusion. EMBO J. *33*, 2745–2764.

Chen, Y.K., and Hsueh, Y.P. (2012). Cortactin-binding protein 2 modulates the mobility of cortactin and regulates dendritic spine formation and maintenance. J. Neurosci. *32*, 1043–1055.

Clarke, J.R., Cammarota, M., Gruart, A., Izquierdo, I., and Delgado-García, J.M. (2010). Plastic modifications induced by object recognition memory processing. Proc. Natl. Acad. Sci. USA *107*, 2652–2657.

Dieterich, D.C., Karpova, A., Mikhaylova, M., Zdobnova, I., König, I., Landwehr, M., Kreutz, M., Smalla, K.H., Richter, K., Landgraf, P., et al. (2008). Caldendrin-Jacob: a protein liaison that couples NMDA receptor signalling to the nucleus. PLoS Biol. *6*, e34.

Faas, G.C., Raghavachari, S., Lisman, J.E., and Mody, I. (2011). Calmodulin as a direct detector of Ca^{2+} signals. Nat. Neurosci. *14*, 301–304.

Gogolla, N., Galimberti, I., DePaola, V., and Caroni, P. (2006). Preparation of organotypic hippocampal slice cultures for long-term live imaging. Nat. Protoc. *1*, 1165–1171.

Gorny, X., Mikhaylova, M., Seeger, C., Reddy, P.P., Reissner, C., Schott, B.H., Helena Danielson, U., Kreutz, M.R., and Seidenbecher, C. (2012). AKAP79/150 interacts with the neuronal calcium-binding protein caldendrin. J. Neurochem. *122*, 714–726.

Helgeson, L.A., and Nolen, B.J. (2013). Mechanism of synergistic activation of Arp2/3 complex by cortactin and N-WASP. elife *2*, e00884.

Hering, H., and Sheng, M. (2003). Activity-dependent redistribution and essential role of cortactin in dendritic spine morphogenesis. J. Neurosci. *23*, 11759–11769.

Honkura, N., Matsuzaki, M., Noguchi, J., Ellis-Davies, G.C., and Kasai, H. (2008). The subspine organization of actin fibers regulates the structure and plasticity of dendritic spines. Neuron *57*, 719–729.

Hotulainen, P., and Hoogenraad, C.C. (2010). Actin in dendritic spines: connecting dynamics to function. J. Cell Biol. *189*, 619–629.

Iki, J., Inoue, A., Bito, H., and Okabe, S. (2005). Bi-directional regulation of postsynaptic cortactin distribution by BDNF and NMDA receptor activity. Eur. J. Neurosci. *22*, 2985–2994.

Kapitein, L.C., Yau, K.W., and Hoogenraad, C.C. (2010). Microtubule dynamics in dendritic spines. Methods Cell Biol. *97*, 111–132.

Karpova, A., Mikhaylova, M., Bera, S., Bär, J., Reddy, P.P., Behnisch, T., Rankovic, V., Spilker, C., Bethge, P., Sahin, J., et al. (2013). Encoding and transducing the synaptic or extrasynaptic origin of NMDA receptor signals to the nucleus. Cell *152*, 1119–1133.

Kim, K., Lakhanpal, G., Lu, H.E., Khan, M., Suzuki, A., Hayashi, M.K., Narayanan, R., Luyben, T.T., Matsuda, T., Nagai, T., et al. (2015). A temporary gating of actin remodeling during synaptic plasticity consists of the interplay between the kinase and structural functions of CaMKII. Neuron *87*, 813–826.

Koskinen, M., and Hotulainen, P. (2014). Measuring F-actin properties in dendritic spines. Front. Neuroanat. *8*, 74.

Loktionov, E.Y., Mikhaylova, M.G., and Sitnikov, D.S. (2016). Experimental Setup for Studying Dynamics of the Calcium Interaction in Cells. Instrum. Exp. Tech. *59*, 601–609.

Longair, M.H., Baker, D.A., and Armstrong, J.D. (2011). Simple Neurite Tracer: open source software for reconstruction, visualization and analysis of neuronal processes. Bioinformatics *27*, 2453–2454.

Martinez-Quiles, N., Ho, H.Y., Kirschner, M.W., Ramesh, N., and Geha, R.S. (2004). Erk/Src phosphorylation of cortactin acts as a switch on-switch off mechanism that controls its ability to activate N-WASP. Mol. Cell. Biol. *24*, 5269–5280.

Matsuzaki, M., Honkura, N., Ellis-Davies, G.C., and Kasai, H. (2004). Structural basis of long-term potentiation in single dendritic spines. Nature *429*, 761–766.

Molnár, E. (2011). Long-term potentiation in cultured hippocampal neurons. Semin. Cell Dev. Biol. *22*, 506–513.

Nägerl, U.V., Novo, D., Mody, I., and Vergara, J.L. (2000). Binding kinetics of calbindin-D(28k) determined by flash photolysis of caged Ca(2+). Biophys. J. *79*, 3009–3018.

Noguchi, J., Hayama, T., Watanabe, S., Ucar, H., Yagishita, S., Takahashi, N., and Kasai, H. (2016). State-dependent diffusion of actin-depolymerizing factor/cofilin underlies the enlargement and shrinkage of dendritic spines. Sci. Rep. *6*, 32897.

Okamoto, K., Narayanan, R., Lee, S.H., Murata, K., and Hayashi, Y. (2007). The role of CaMKII as an F-actin-bundling protein crucial for maintenance of dendritic spine structure. Proc. Natl. Acad. Sci. USA *104*, 6418–6423.

Okamoto, K., Bosch, M., and Hayashi, Y. (2009). The roles of CaMKII and F-actin in the structural plasticity of dendritic spines: a potential molecular identity of a synaptic tag? Physiology (Bethesda) *24*, 357–366.

Racz, B., and Weinberg, R.J. (2004). The subcellular organization of cortactin in hippocampus. J. Neurosci. *24*, 10310–10317.

Racz, B., and Weinberg, R.J. (2006). Spatial organization of cofilin in dendritic spines. Neuroscience *138*, 447–456.

Rácz, B., and Weinberg, R.J. (2013). Microdomains in forebrain spines: an ultrastructural perspective. Mol. Neurobiol. *47*, 77–89.

Raghuram, V., Sharma, Y., and Kreutz, M.R. (2012). $Ca^{(2+)}$ sensor proteins in dendritic spines: a race for $Ca^{(2+)}$. Front. Mol. Neurosci. *5*, 61.

Reddy, P.P., Raghuram, V., Hradsky, J., Spilker, C., Chakraborty, A., Sharma, Y., Mikhaylova, M., and Kreutz, M.R. (2014). Molecular dynamics of the neuronal EF-hand Ca^{2+}-sensor Caldendrin. PLoS ONE *9*, e103186.

Sabatini, B.L., Oertner, T.G., and Svoboda, K. (2002). The life cycle of $Ca^{(2+)}$ ions in dendritic spines. Neuron *33*, 439–452.

Schätzle, P., Kapitein, L.C., and Hoogenraad, C.C. (2016). Live imaging of microtubule dynamics in organotypic hippocampal slice cultures. Methods Cell Biol. *131*, 107–126.

Schindelin, J., Arganda-Carreras, I., Frise, E., Kaynig, V., Longair, M., Pietzsch, T., Preibisch, S., Rueden, C., Saalfeld, S., Schmid, B., et al. (2012). Fiji: an open-source platform for biological-image analysis. Nat. Methods *9*, 676–682.

Schnoor, M., Stradal, T.E., and Rottner, K. (2018). Cortactin: cell functions of a multifaceted actin-binding protein. Trends Cell Biol. *28*, 79–98. Published online November 20, 2017.

Seese, R.R., Babayan, A.H., Katz, A.M., Cox, C.D., Lauterborn, J.C., Lynch, G., and Gall, C.M. (2012). LTP induction translocates cortactin at distant synapses in wild-type but not Fmr1 knock-out mice. J. Neurosci. *32*, 7403–7413.

Seidenbecher, C.I., Langnaese, K., Sanmartí-Vila, L., Boeckers, T.M., Smalla, K.H., Sabel, B.A., Garner, C.C., Gundelfinger, E.D., and Kreutz, M.R. (1998). Caldendrin, a novel neuronal calcium-binding protein confined to the somato-dendritic compartment. J. Biol. Chem. *273*, 21324–21331.

Sjöblom, B., Ylänne, J., and Djinović-Carugo, K. (2008). Novel structural insights into F-actin-binding and novel functions of calponin homology domains. Curr. Opin. Struct. Biol. *18*, 702–708.

Spilker, C., Nullmeier, S., Grochowska, K.M., Schumacher, A., Butnaru, I., Macharadze, T., Gomes, G.M., Yuanxiang, P., Bayraktar, G., Rodenstein, C., et al. (2016). A Jacob/Nsmf Gene Knockout Results in Hippocampal Dysplasia and Impaired BDNF Signaling in Dendritogenesis. PLoS Genet. *12*, e1005907.

Star, E.N., Kwiatkowski, D.J., and Murthy, V.N. (2002). Rapid turnover of actin in dendritic spines and its regulation by activity. Nat. Neurosci. *5*, 239–246.

Tsuriel, S., Geva, R., Zamorano, P., Dresbach, T., Boeckers, T., Gundelfinger, E.D., Garner, C.C., and Ziv, N.E. (2006). Local sharing as a predominant determinant of synaptic matrix molecular dynamics. PLoS Biol. *4*, e271.

van Spronsen, M., Mikhaylova, M., Lipka, J., Schlager, M.A., van den Heuvel, D.J., Kuijpers, M., Wulf, P.S., Keijzer, N., Demmers, J., Kapitein, L.C., et al. (2013). TRAK/Milton motor-adaptor proteins steer mitochondrial trafficking to axons and dendrites. Neuron *77*, 485–502.

Wiegert, J.S., Gee, C.E., and Oertner, T.G. (2017). Single-Cell Electroporation of Neurons. Cold Spring Harb. Protoc. https://doi.org/10.1101/pdb.prot094904.

STAR★METHODS

KEY RESOURCES TABLE

REAGENT or RESOURCE	SOURCE	IDENTIFIER
Antibodies		
Rabbit anti-Caldendrin	Dr. Pineda antibody service; (Dieterich et al., 2008)	N/A
Guinea pig anti-Caldendrin	Dr. Pineda antibody service, (Dieterich et al., 2008)	N/A
rabbit anti-cortactin	Santa Cruz	H-191; Cat#Sc-11408; RRID:AB_2088281
mouse anti-Arp2	Santa Cruz	clone B-6; Cat#sc-376698; RRID:AB_11150655
rabbit anti-N-WASP	Santa Cruz	H-100; Cat#sc-20770; RRID:AB_2288632
rabbit anti-GFP	Abcam	Cat#ab6556; RRID:AB_305564
rat anti-HA	Roche	Cat#11867423001; RRID:AB_390918
rabbit anti-RFP	Rockland Immunochemicals	Cat#600-401-379; RRID:AB_2209751
rabbit anti-MAP2	Synaptic Systems	Cat#188011; RRID:AB_2147096
rabbit anti-synapsin	Synaptic Systems	Cat#106002; RRID:AB_887804
guinea pig anti-synaptophysin	Synaptic Systems	Cat#101004; RRID:AB_1210382
mouse anti-bassoon	Stressgen, now Enzo	Clone SAP7F407; Cat#ADI-VAM-PS003; RRID:AB_10618753
mouse anti- PSD95	BD Transduction Laboratories	Clone 16/PSD-95; Cat#610496; RRID:AB_397862
mouse anti- β-III-tubulin	Sigma-Aldrich	clone SDL.3D10; Cat#T8660; RRID:AB_477590
mouse anti-Shank2	UC Davis, NIH NeuroMab Facility	Clone N23B/6; Cat#75-088; RRID:AB_2254586
Rabbit anti-GluR1	Millipore	Cat#PC246; RRID:AB_564636
Mouse anti-homer	Synaptic Systems	Cat#160011; RRID:AB_2120992
anti-mouse-Alexa Fluor 488	Thermo Fisher Scientific	Cat#A-11001; RRID:AB_2534069
anti-mouse-Alexa Fluor 568	Thermo Fisher Scientific	Cat#A-11004; RRID:AB_2534072
anti-mouse-Alexa Fluor 647	Thermo Fisher Scientific	Cat#A-21235; RRID:AB_2535804
anti-rabbit-Alexa Fluor 488	Thermo Fisher Scientific	Cat#A-11034; RRID:AB_2576217
anti-rabbit-Alexa Fluor 568	Thermo Fisher Scientific	Cat#A-11036; RRID:AB_10563566
anti-rabbit-Alexa Fluor 647	Thermo Fisher Scientific	Cat#A-21236; RRID:AB_2535805
anti-guinea pig-Alexa 488	Thermo Fisher Scientific	Cat#A-11073; RRID:AB_2534117
anti-guinea pig-Alexa 568	Thermo Fisher Scientific	Cat#A-11075; RRID:AB_2534119
anti-guinea pig-Alexa 647	Thermo Fisher Scientific	Cat#A-21450; RRID:AB_2535867
anti-mouse Abberior Star 580	Abberior	Cat#2-0002-005-1; RRID:AB_2620153
anti-rabbit-HRP	CST	Cat#7047; RRID:AB_2099233
anti-rabbit-HRP	Dianova Jackson ImmunoResearch	Cat#111-035-144; RRID:AB_2307391
anti-mouse HRP	Dako	Cat#P0447; RRID:AB_2617137
anti-mouse HRP	Dianova Jackson ImmunoResearch	Cat#115-035-146; RRID:AB_2307392
Bacterial and Virus Strains		
E.coli XL10Gold	Agilent	Cat#200314
E.coli Bl21DE3	Invitrogen	Cat#C6000-03
Lenti virus	this paper; (Schätzle et al., 2016)	N/A

(*Continued on next page*)

Continued

REAGENT or RESOURCE	SOURCE	IDENTIFIER
Chemicals, Peptides, and Recombinant Proteins		
Phalloidin–Atto647N	Sigma-Aldrich	Cat#65906-10NMOL
bicuculline	Tocris	Cat#2503
jasplakinolide	Tocris	Cat#2792
picrotoxin	Tocris	Cat#1128
brain derived neurotrophic factor (rhBDNF)	Promega	Cat#G1491
ionomycin	Calbiochem	Cat#407952-1MG
DM-Nitrophen	Calbiochem	Cat#317210
Oregon Green 488 BAPTA-5N	Thermo Fisher Scientific	Cat#O6812
Tetrodotoxin	Tocris	Cat#1078
Human recombinant cofilin	Cytoskeleton	Cat#CF01-A
CaM	Sigma Aldrich	Cat#C4874
Arp2/3	Cytoskeleton	Cat#RP01P
NWASP	Cytoskeleton	Cat#VCG03-A
Actin 568	Thermo Fisher Scientific	Cat#A12374
PLL(20)-g[3.5]- PEG(2)/PEG(3.4)- biotin(50%)	Susos AG	N/A
neutravidin	Thermo Fisher Scientific	Cat#31000
ATP	Sigma Aldrich	Cat# A2383-5G
Catalase	Sigma Aldrich	Cat#C40
Glucose Oxidase	Sigma Aldrich	Cat#G2133
Fluo 5F	Thermo Fisher Scientific	Cat#F14221
Alexa Fluor-594	Thermo Fisher Scientific	Cat#A10438
Gluthation Sepharose	GE	Cat#17075601
Chitin Magnetic Beads	NEB	Cat#E8036
GFP-trap_MA	chromotek	Cat#gtma
Prot A beads	Biorad	Cat#161-4013
Prot G beads	Biorad	Cat#161-4023
Lipofectamine 2000	Invitrogen	Cat#11668027
MaxPEI	Polysciences	Cat#23966
Polyfect	QIAGEN	Cat#301105
Fugene6	Promega	Cat#E2691
Critical Commercial Assays		
TranSignal SH3 domain array I	Panomics Inc	Cat#MA3010
actin from *in vitro* assay pyrene-actin	Cytoskeleton	Cat#BK003
Magnetic beads	Miltenyi Biotec	Cat#130-91-125
Experimental Models: Cell Lines		
Human: HEKT-293	Leibniz Institute DSMZ	ACC 635
Human: HEKT-293	ATCC	CRL-3216
African Green Monkey SV40-transformed kidney fibroblast (COS-7)	ATCC	CRL-1651
Experimental Models: Organisms/Strains		
Mouse: *cald*$^{-/-}$	this paper	N/A
Rat: Wistar	Charles River	Crl:WI(Han)
Rat: Wistar	Janvier	RjHan:WI
Oligonucleotides		
Genotyping: Cald_wt_F: GGGGAGGGTGAT CCGATGTCTC	this paper	N/A
Genotyping: Cald_wt_R: GGATTTTCCTGTC TCTGACTCCTCA	this paper	N/A

(*Continued on next page*)

Continued

REAGENT or RESOURCE	SOURCE	IDENTIFIER
Genotyping: LTR2_mut-F: ATGGCGTTACTT AAGCTAGCTTGC	this paper	N/A
RT PCR primer: CALD_ex1_5UTR: 5'CAGC GCGTCCTCGGGCTTG	this paper	N/A
RT PCR primer: CaBP1_ex1A_5UTR: GCCT CCTTCATGGACCCAGAGAC	this paper	N/A
RT PCR primer: CaBP1_ex7_3UTR: CTGTG GGAGTTGGCAGACCTG	this paper	N/A
RT PCR primer: CALD_ex1: ATGAGCTCGC ACATTGCCAAG	this paper	N/A
RT PCR primer: CaBP1_ex1A: ATGGGCAA CTGCGTCAAGTCG	this paper	N/A
RT PCR primer: CaBP1_ex7: 5TCAGCGAG ACATCATCCGGAC	this paper	N/A
RT PCR primer: actin_fwd: GAGCGTGGCT ACAGCTTCACC	this paper	N/A
RT PCR primer: actin_rev: CGTACTCCTG CTTGCTGATCCAC	this paper	N/A
Recombinant DNA		
pEGFP-N1	Clontech	Cat#6085-1
pEGFP-C1	Clontech	Cat#6084-1
pmCherry-N1	Clontech	Cat#632523
pmCherry-C1	Clontech	Cat#632524
pcDNA3.1myc-His(-)A	Thermo Fisher Scientific	Cat#V855-20
pcDNA3.1(+)	Thermo Fisher Scientific	Cat#V790-20
pGHEB	(Dieterich et al., 2008)	N/A
shRNA_cald#1 (GGCCGCATTTAAGCGGC CA) in psi-H1	Genecopoeia	N/A
shRNA_cald#2 (AGAGCGAGTCCAAGACG TC) in psi-H1	Genecopoeia	N/A
shRNA_cald#3 (GTCAGGATAGATCGTTA CG) in psi-H1	Genecopoeia	N/A
shRNA_cald#4 (CCAGCAGATCAACATG AAC) in psi-H1	Genecopoeia	N/A
mYFP-mCFP in pGW1	(van Spronsen et al., 2013)	N/A
mYFP in pGW1	(van Spronsen et al., 2013)	N/A
mCFP in pGW1	(van Spronsen et al., 2013)	N/A
caldendrin in pEGFP-N1	(Dieterich et al., 2008)	N/A
shRNA_scr in pRNAt	(Dieterich et al., 2008)	N/A
shRNA_cald#5 in pRNAt (TCC TGG CGG AGA CAG CAG ATA	(Dieterich et al., 2008)	N/A
shRNA_cort in pSUPER	this paper	N/A
beta-galactosidase-HA in p-beta-actin	(van Spronsen et al., 2013)	N/A
full-length caldendrin in pMXB10	(Reddy et al., 2014)	N/A
cald-Nt (aa 1-136) in pEGFP-N1	(Reddy et al., 2014)	N/A
cald-Ct (aa 137-298) in pEGFP-N1	(Reddy et al., 2014)	N/A
YFP-caldendrin-CFP in pGW1	(Reddy et al., 2014)	N/A
mCherry-cortactin-C-12	a gift from Michael Davidson	Addgene plasmid # 55020
GFP-C1-CAMKIIbeta	a gift from Tobias Meyer	Addgene plasmid # 21227
pAAV-hSyn1-mRuby2	a gift from Simon Wiegert	N/A

(*Continued on next page*)

Continued

REAGENT or RESOURCE	SOURCE	IDENTIFIER
pAAV-hSyn1-eYFP	this paper	N/A
6xHis-SUMO-Caldendrin-Nt (aa 1-136)	this paper	N/A
GST-cortactin in pGHEB	this paper	N/A
GST-cortactin-SH3 in pGHEB	this paper	N/A
Caldendrin-R40,41A-GFP in pEGFP-N1	this paper	N/A
Caldendrin calcium binding mutant constructs in pcDNA3.1+(D243A D280A)	this paper	N/A
Caldendrin calcium binding mutant constructs in pMXB10 (D243A D280A)	this paper	N/A
GFP-actin in pbeta-actin	this paper	N/A
YFP-cortactin-CFP in pGW1	this paper	N/A
Cald_1-60 in pMXB10	this paper	N/A
cald-EF3-4 in pMXB10	this paper	N/A
Caldendrin-myc in pcDNA3.1myc-His(-)A	this paper	N/A
EGFP-cortactin in pEGFP-C1	this paper	N/A
shRNA#5-Cald_rescue-GFP pRNAt	this paper	N/A
Lentivirus shRNA constructs: scrambled GGT TTATATCGCGGTTATT in pSIN-TREMARCKS-GFP-H1-shRNA	this paper	N/A
Lentivirus shRNA constructs: Cortactin GCACT GCTCACAAGTGGAC n pSIN-TREMARCKS-GFP-H1-shRNA	this paper; (Hering and Sheng, 2003)	N/A
Lentivirus shRNA constructs: Caldendrin#5 in pSIN-TREMARCKS-GFP-H1-shRNA	this paper	N/A
GFP-Caldendrin-GFP in pEGFP	this paper	N/A
mCherry-GFP in pbeta-actin	this paper	N/A
Software and Algorithms		
MATLAB Version R2015a	MathWorks	https://www.mathworks.com; RRID: SCR_001622
(Fiji is just) ImageJ Version 1.49v	(Schindelin et al., 2012)	http://fiji.sc/; RRID:SCR_002285
Openview Version 1.5	(Tsuriel et al., 2006)	N/A
Prism Version 6.05	GraphPad	https://www.graphpad.com/scientific-software/prism/
Imaris version 7.7.1	Bitplane	http://www.bitplane.com/imaris/imaris; RRID:SCR_007370
Origin 2018	OriginLab	https://www.originlab.com
custom script for STED analysis (MATLAB)	this paper	N/A
Patchmaster version 2x73.5	HEKA Elektronik	http://www.heka.com/
Fitmaster version 2x90.2	HEKA Elektronik	http://www.heka.com/
Minianalysis version 6.0.3	Synaptosoft	http://www.synaptosoft.com/MiniAnalysis/
ANY-maze video tracking version 4.50	Stoelting Co.	http://www.anymaze.co.uk/

CONTACT FOR REAGENT AND RESOURCE SHARING

Further information and requests for resources and reagents should be directed to and will be fulfilled by the Lead Contact, Michael R. Kreutz (kreutz@lin-magdeburg.de).

EXPERIMENTAL MODEL AND SUBJECT DETAILS

Animals

All animal experiments were carried out in accordance with the European Communities Council Directive (2010/63/EU) and the Animal Welfare Law of the Federal Republic of Germany (Tierschutzgesetz der Bundesrepublik Deutschland, TierSchG) approved by the local authorities of Sachsen-Anhalt/Germany (reference number 42502-2-987IfN and 42502-2-1264 LIN, TV 42502-2-1009 UniMD) or of the city-state Hamburg (Behörde für Gesundheit und Verbraucherschutz, Fachbereich Veterinärwesen) and the animal care committee of the University Medical Center Hamburg-Eppendorf. The animals used in this study were bred and maintained in the animal facility of the Leibniz Institute for Neurobiology, Magdeburg, Germany or ZMNH, Hamburg, Germany. Animals were housed in individually ventilated cages (Green line system, Tecniplast) in groups of up to 5 animals with free access to food and water under controlled environmental conditions (22 ± 2°C, 55% ± 10% humidity, 12 h, light–dark cycle, with lights on at 06:00 a.m.).

Sex as well as the age/developmental stage of experimental animals are indicated in the Method Details (Neuronal culture, transfections and lentiviruses; Organotypic hippocampal slice cultures; Electrophysiology in acute hippocampal slices; Behavior).

Generation of caldendrin-knockout mice

Caldendrin knockout mice were obtained from the Texas A&M Institute for Genomic Medicine (Houston, USA). Knockout mice were generated using the OmniBank ES cell clone OST258109 derived from the 129SvEv strain. Gene-trap insertion in this clone was mapped to mouse chromosome 5, 448 bp downstream of exon 2 of the Caldendrin / CaBP1 gene. Mice used for experiments were backcrossed for at least 10 generations to C57BL/6J and derived from heterozygous breedings. Verification of genotypes was done using the following primers: Cald_wt_F: GGGGAGGGTGATCCGATGTCTC, Cald_wt_R: GGATTTTCCTGTCTCTGACTCCTCA, LTR2_mut-F: ATGGCGTTACTTAAGCTAGCTTGC. Expression of caldendrin and its short isoforms was tested by RT-PCR. RNA was extracted from mouse hippocampus and retina using a rotating tissue homogenizer and the RNeasy Mini Kit (QIAGEN GmbH, Hilden, Germany) following the manufacturer's instructions. Reverse transcription was performed with Omniscript (QIAGEN) using Oligo(dT) primers for 1 h at 37°C. Caldendrin and CaBP1 cDNAs were amplified in two PCRs using nested primers in the second. In detail the following primers were used: 1. PCR, for Caldendrin CALD_ex1_5UTR 5'CAGCGCGTCCTCGGGCTTG; for CaBP1 CaBP1_ex1A_5UTR GCCTCCTTCATGGACCCAGAGAC and a common reverse primer CaBP1_ex7_3UTR CTGTGGGAGTTGGCAGACCTG (25 cycles; 95°C for 45 s; 59°C for 45 s, 72°C for 90 s); 2. PCR (nested) for Caldendrin CALD_ex1 ATGAGCTCGCACATTGCCAAG; for CaBP1 CaBP1_ex1A ATGGGCAACTGCGTCAAGTCG and a common reverse primer CaBP1_ex7 5TCAGCGAGACATCATCCGGAC (20 cycles 95°C for 45 s; 61°C for 45 s, 72°C for 90 s). As controls primers specific for mouse actin were used (GAGCGTGGCTA CAGCTTCACC; CGTACTCCTGCTTGCTGATCCAC). PCR constructs were verified by sequencing.

Cell culturing conditions

COS-7 and HEK293T cells were maintained in Dulbecco's modified Eagle's medium (DMEM) supplemented with 10% fetal calf serum (FCS), 1 x penicillin/ streptomycin, 2 mM glutamine at 37°C, 5% CO_2 and 95% humidity.

METHOD DETAILS

Antibodies

Rabbit and guinea pig caldendrin antibodies were generated by the Dr. Pineda antibody service, affinity purified and characterized as described previously (Dieterich et al., 2008) (immunofluorescence, IF 1:100, WB 1:1000). The following commercial primary and secondary antibody we used in this study: rabbit anti-cortactin (IF 1:200), mouse anti-Arp2 (WB 1:200), rabbit anti-N-WASP (WB 1:100) from Santa Cruz; rabbit anti-GFP (WB 1:2000) from Abcam; rat anti-HA (IF 1:500) from Roche; rabbit anti-RFP (western blotting, WB 1:1000) from Rockland Immunochemicals; rabbit anti-MAP2 (IF 1:500), rabbit anti-synapsin (IF 1:800), guinea pig anti-synaptophysin (IF 1:500) from Synaptic Systems; mouse anti-bassoon (IF 1:500) from Stressgen; mouse anti-PSD95 (WB 1:2000) from BD Transduction Laboratories; mouse anti- β-III-tubulin (WB 1:1000) from Sigma-Aldrich, mouse anti-Shank2 (IF 1:500) from UC Davis, NIH NeuroMab Facility; secondary anti-mouse, anti-rabbit and anti-guinea pig antibodies labeled with Alexa Fluor 488, Alexa Fluor 568 or Alexa Fluor 647 (IF 1:500) from Molecular Probes (Invitrogen); anti-mouse Abberior Star 580 (IF 1:200) from Abberior; secondary anti-rabbit and anti-mouse HRP-conjugated antibody (WB 1:5000 – 1:20000) from Dako and Dianova.

Constructs

shRNA resistant mutants of caldendrin were created by replacement of TCCTGGCGGAGACAGCAGATA by TATTAGCAGAAACG GCCGAAA via creation of PCR fragments overlapping in the particular region with subsequent cold fusion into the linearized pRNAt vector.

pAAV-hSyn1-mRuby2 created by excision of GCaMP6f from pAAV-hSyn1-mRuby2-GSG-P2A-GCaMP6f-WPRE-pA (Addgene plasmid # 50943) was a gift from Simon Wiegert.

Lentivirus was based on the pSIN-TRE-mSEAP-hPGK-rtTA2sM2 vector (Didier Trono, EPFL). The hPGK promoter was replaced by the 0.5kb synapsin promoter and mSEAP was exchanged for MARCKS-GFP. Constitutive shRNA knock down is archieved by

subcloning the H1 promoter and shRNA sequence from the original pSuper constructs behind the WPRE region (Figure S6A). The following shRNAs sequences were inserted: scrambled GGTTTATATCGCGGTTATT, Cortactin GCACTGCTCACAAGTGGAC (Hering and Sheng, 2003) and Caldendrin#5.

Biochemistry

Brain lysates, subcellular fractionation and WB

Freshly dissected tissue from adult *cald*$^{+/+}$ and $^{-/-}$ mice or Wistar rats was shortly rinsed in phosphate buffer saline (PBS) and then snap frozen in liquid nitrogen and stored at −80°C. Homogenization was done in buffer containing 10 mM Tris/HCl pH 7.5, 0.5% Triton X-100 and complete protease inhibitor cocktail (PI, Roche Diagnostics) using a hand homogenizer in a ratio of 10 ml/g wet weight. Tissue homogenates were then mixed with 4x SDS sample buffer (250 mM Tris pH 8.5, 8% SDS, 40% glycerol, 2 mM EDTA, 0.01% bromphenol blue, 100 mM dithiothreitol (DTT)) in a ratio of 2:1, boiled for 10 min and centrifuged at 17000 x g for 5 min. Total protein concentration of supernatants was determined by amido black protein assay and equal amounts of tissue extracts (15 or 20 μg per lane) were loaded for SDS-PAGE on 4%–12% gradient gels and blotted onto nitrocellulose or PVDF membranes. After blocking in 5% skim milk in Tris-buffered saline / Tween (TBS-T, 20 mM Tris, 150 mM NaCl, pH 7.4, 0.1% Tween-20) or 5% BSA in TBS-T membranes were incubated with primary antibodies diluted in TBS-A (TBS+ 0.02% NaN_3 pH 7.4) overnight at 4°C. Corresponding HRP-conjugated secondary antibody were applied for 1-1.5 h at room temperature (RT). For quantification of caldendrin protein amount in brain purified full-length caldendrin (untagged) in different amount was used as quantification standards. Proteins were detected using rabbit anti-caldendrin antibody. Quantification of proteins was performed using the ImageJ implemented gel analyzer (NIH). Subcellular fractionation of rat cortex and hippocampus was performed as described earlier (Karpova et al., 2013). Protein concentration was measured by amido black assay and 20 μg of each fraction were loaded per lane. PSD-95 was used as positive control for preparation.

Protein purification from E. coli

Expression and purification of GST-tagged cortactin-full-length and SH3 domain was generally performed as (Reddy et al., 2014). Briefly, GST-tagged constructs were expressed in *E. coli* BL21 (DE3). After 6 h of induction with 0.5 mM isopropyl-beta-D-thiogalactoside at 37°C cells were pelleted by centrifugation at 6.000 x g for 15 min and purified from the soluble fraction by glutathione-Sepharose chromatography. Untagged wild-type and calcium binding mutant of caldendrin and the shorter fragments of the wild-type protein were produced using the intein system as described previously (Reddy et al., 2014), 6xHis-SUMO-tagged caldendrin N terminus was purified as described previously for other 6xHis-SUMO-tagged caldendrin constructs (Gorny et al., 2012). Depending on degree of purity recombinant proteins were passed through a superdex 75 gel filtration column using an ÄKTA FPLC system (ÄKTA purifier, GE Healthcare).

For protein conformational analysis and proper folding, 8-Anilinonaphthalene-1-sulfonate fluorescence spectroscopy was performed as described previously (Reddy et al., 2014). Purified caldendrin was decalcified using 100 μM EDTA followed by buffer exchange to Chelex-100 (BioRad) treated with 50 mM Tris, 100 mM KCl, pH 7.4. 0.5 mM $MgCl_2$ was added to the EDTA treated protein solution and further buffer exchange was done to remove unbound Mg^{2+}, and subsequently lyophylized using a FreeZone freeze dry system (Labconco). Lyophilized protein was reconstituted in Chelex-100 treated deionized water.

SH3-domain array

TranSignal SH3 domain array I of human GST-SH3 domain fusion proteins spotted in duplicate was purchased from Panomics Inc. 6xHis-SUMO-cald-Nt was purified from *E. coli* as described above and 1.5 μg/ml of the recombinant protein were used for binding. The assay was performed according to manufacturer's instructions. Shortly, the SH3 array membrane was blocked in 5% non-fat milk and incubated with purified 6xHis-SUMO-cald-Nt 4°C over night, washed and incubated with anti-histidine HRP conjugate for 1-2 h at RT. Signal was detected after additional washing steps using provided detection buffer and exposure to hyperfilm.

GST pull-down assays

Sepharose-bound GST-cortactin or GST was used for pull-down assays. Caldendrin constructs were heterologously expressed in HEK293T cells. Sepharose beads were washed with the corresponding Ca^{2+} buffer (2 mM $CaCl_2$, 1 mM $MgCl_2$ in TBS, pH 7.4) or a Ca^{2+} free buffer (2 mM EGTA, 1 mM $MgCl_2$, in TBS, pH 7.4) and pre-incubated with 5% bovine serum albumin at 4°C for 30 min to reduce non-specific binding. Then the beads were washed and incubated for 4 h at 4°C with cell extracts prepared in respective buffer. After extensive washing with corresponding buffers protein samples were eluted with 2x SDS sample buffer and proceeded for immunoblotting.For the pull down using two purified proteins, GST tagged cortactin and GST alone was immobilized on GST beads and incubated with equimolar caldendrin at 4°C for 3 hr in presence of 10 μM Ca^{2+}/EGTA. Samples were washed with cold buffer 50 mM Tris (pH 7.4), 150 mM NaCl, 0.1% Tween 20, 1 mM DTT containing either 10 μM Ca^{2+} or 10 μM EGTA. Proteins were eluted using 2X SDS-PAGE loading buffer, SDS-PAGE gel was run and blot was developed using caldendrin antibody.

Heterologous co-immunoprecipitations

For co-immunoprecipitation experiments different combinations of mCherry-cortactin, GFP-cortactin and untagged caldendrin or GFP tagged truncated constructs of caldendrin and corresponding GFP and mCherry controls, were heterologously expressed in COS-7 cells. Cells were harvested and proteins were extracted with Triton X-100 containing TBS buffer [1% (v/v) Triton X-100, 20 mM Tris, 150 mM NaCl and 2 mM DTT, pH 7.4] 48 h after transfection. Cell extracts were obtained by centrifucation at 12000 x g for 30 min at 4°C and incubated for 1 h at 4°C with anti-GFP antibodies coated on magnetic beads (Miltenyi Biotec) in Ca^{2+}-buffer [2 mM $CaCl_2$, 1 mM $MgCl_2$, 1% (v/v) Triton X-100, 20 mM Tris, 150 mM NaCl and 2 mM DTT, pH 7.4] or EGTA-buffer

[2 mM EGTA, 1 mM $MgCl_2$, 1% (v/v) Triton X-100, 20 mM Tris, 150 mM NaCl and 2 mM DTT, pH 7.4]. Magnetic beads were extensively washed and protein complexes were eluted according to the manufacturer's protocol (Miltenyi Biotec). The immunoprecipitation of proteins was checked with anti-caldendrin, anti-RFP and anti-GFP antibodies.

For immunoprecipitation of endogenous N-WASP complex, HEK293 cells were transfected with GFP-cortactin or GFP with or without caldendrin in pcDNA3.1 for 24 h, then cells were harvested and lysed in a buffer containing 0.5% (v/v) Triton X-100, 20 mM Tris pH 8.0, 150 mM NaCl, 2 mM $MgCl_2$ and protease inhibitor cocktail. Mixture of Protein A and Protein G magnetic beads (Biorad) were incubated with anti-rabbit N-WASP antibody (Santa Cruz) in the presence of 0.2% of chicken egg white for 2 h, then washed with the extraction buffer and added to the cell extracts supplemented either with 2 mM EGTA or 0.2 mM $CaCl_2$. After overnight incubation at 4°C beads were extensively washed and eluted using 2x SDS sample buffer.

The interaction of cortactin with caldendrin calcium binding mutant was investigated by immunoprecipitation with GFP-trap_MA (Chromotek). GFP-Cortactin or GFP were co-expressed with wild-type caldendrin or calcium binding mutant in HEK293 cells for 24h. Cells were harvested and lysed as described above. GFP-trap_MA beads magnetic beads were blocked with 0.2% of chicken egg white in TBS for 30 min at RT. Cell extracts supplemented with 2 mM EGTA or 0.5 mM $CaCl_2$ were added and incubated at 4°C ON. After extensive washing beads were eluted using 2x SDS sample buffer.

Biophysics

UV flash photolysis

To analyze the dynamics of Ca^{2+} binding to Mg^{2+}-bound caldendrin we used UV uncaging of DM-Nitrophen. The experimental setup was constructed at ''Beam-M'' research facility, BMSTU and described in detail earlier (Loktionov et al., 2016). Flash-photolysis of Ca^{2+}-loaded DM-Nitrophen (Millipore) was induced by frequency tripled (355 nm) nanosecond (7 ns) Nd:YAG laser (Solar LS LQ-115). Photoluminescense was excited by 5 ms (or longer) pulses of 473 nm DPSS laser (Lasever LSR473), starting 1 ms earlier than photolysis (BNC 575 pulse generator was used for synchronization). Oregon Green 488 BAPTA-5N (OGB-5N; Thermo Fisher Scientific) fluorescence was band filtered (using Thorlabs FEL0500, FES0550, FES0600) to get a pure 525 ± 25 nm band, and recorded using PMT (Hamamatsu H6420) coupled with a digital oscilloscope (Tektronix DPO7254). To cut off 355 nm signal, we used a 100 kHz short pass signal filter (Thorlabs EF502) in addition to optical ones. Ca^{2+} uncaging was performed in 5 μL droplets of solutions placed on a sample glass. Photoluminescence exitation radiation (473 nm) was transported using a light source leg of a probe bundle (Thorlabs RP28) coupled with achromatic adaptor (Solar LS FA-2), and induced radiation was collected by peripherial fibers. Achromatic condenser (Solar LS PS-2) on a 3D-mount was used for focusing to get maximum of photoluminescence signal. The spectrometer leg was used to supply that signal to PMT after passing through the above mentioned edge filters and coupling with another round-to-linear bundle (Thorlabs BFL105HS02). Thorlabs cage system elements and achromatic fiber adapters were used in this construction. The composition of experimental groups is given in Table S3. Calmodulin was purchased from Sigma, caldendrin was expressed and purified from *E. coli* as described above. All reagents were freshly dissolved directly before the measurements. Kinetic parameters of calcium binding to caldendrin or EGTA (t_{decay}) were analyzed as described in (Nägerl et al., 2000).

Isothermal titration calorimetery

Isothermal titration calorimetery (ITC) was performed using a Microcal VP-ITC calorimeter to check the Ca^{2+} binding to caldendrin and the calcium binding mutant at 25°C in chelex treated 50 mM Tris buffer (pH 7.4) containing 100 mM NaCl. 35 μM Mg^{2+}-bound protein was titrated against 10 mM $CaCl_2$ prepared in same buffer. Experiments consist of injections 5 μl of Ca^{2+} each separated by 3 min of equilibration period. Only buffer and Ca^{2+} titration were also performed to measure heat of dilution and subtracted from protein samples. Heat change i.e., binding enthalpy was calculated by integrating the area under peaks and for the time course of power change and further other thermodynamic parameters was derived from that and fitted with different binding models provided by inbuilt origin software.

Surface plasmon resonance analysis

Binding and protein complex stability studies for the untagged full-length caldendrin or calcium binding mutant of caldendrin and GST-cortactin were carried out on a sensor chip CM5 using the Biacore X-100 instrument (Biacore AB, GE Healthcare, Uppsala, Sweden) at 25°C according to the manufacturer's instructions. Briefly, after equilibrating the sensor chip with flow buffer HBS-P (10 mM HEPES pH 7.4, 150 mM NaCl, 0.005% Surfactant P20) at a flow rate of 10 μl/min, the Dextran matrix was activated with a 7-minute pulse of 50 mM N-hydroxysuccinimide/200 mM N-ethyl-N'-(dimethylaminopropyl)- carbodiimide at a flow rate of 10 μl/min. Subsequently caldendrin full-length was immobilized at the surface of the sensor chip cell by injecting a 7-minute pulse of ligand solution (20 μg/ml of each). Finally the excess of reactive groups on the chip surface was deactivated with a 7-minute pulse of 1 M ethanolamine hydrochloride pH 8.5, at a flow rate of 10 μl/min. For binding and complex stability studies GST-cortactin-SH3 (5 μM) was injected on the immobilized caldendrin full-length surface diluted in the continuous flow buffer HBS-P containing either 1 mM $CaCl_2$ or 1 mM EGTA. Injections were done in a 3-minute pulse (association time) followed by a 3-minute pulse with analysis buffer alone (dissociation time) and sensorgram was recorded for 60 min at flow rate of 10 μl/min. For protein complex stability analysis stability points were taken 30 min and 60 min after the first stability point.

For measuring binding kinetics between full length caldendrin and cortactin at physiological [Ca^{2+}], polyclonal goat anti-GST antibody was immobilized on CM5 chip surface as per standard protocol provided by GST capture kit (GE healthcare) followed by blocking minor fraction of high affinity sites that are difficult to regenerate. Assay condition for both ligand GST-cortactin and analyte caldendrin was assayed. Thereafter binding affinity between cortactin and caldendrin was measured in HBSP running buffer

containing 10 μM $CaCl_2$. Association and dissociation constants were calculated using steady state affinity model of Biacore X100 BIAevaluation software by picking the point at position 4 s before injection stops.

For testing the interaction between caldendrin-Nt (60 amino acid (aa)) with its second EF-domain, caldendrin EF-2 domain was immobilized on CM5 chip as described above. Untagged caldendrin Nt (1-60aa) was injected as analyte in the continuous flow of HBS-P running buffer containing either 1 mM $CaCl_2$ or 1 mM EGTA. Experiments were repeated four times and quantification was done using maximum binding points and stability points. SH3 domain of cortactin was immobilized on CM5 chip surface and association rate of caldendrin interaction was calculated by passing over caldendrin (in presence of 500 μM Ca^{2+} or EGTA in HBSP buffer) and fitting the obtained data using BIAevaluation software.

In vitro actin assays

F-actin sedimentation assay in HEK293T cells

F-actin sedimentation assays were performed to study the role of caldendrin on the F- to G-actin ratio. HEK293T cells were transiently transfected with caldendrin-pcDNA3.1 or empty pcDNA3.1 vector as a control. As positive control untransfected HEK293T cells were pre-treated with 50 nM JPK or DMSO for 3 hours. Harvesting was done in 500 μl of prewarmed buffer containing TBS (20 mM Tris pH 7.4 and 150 mM NaCl), protease inhibitor cocktail (Roche), 1% Triton X-100, 100 μM ATP, and 50 nM JPK to protect existing filaments from depolymerization. After centrifugation the remove cell debris, the supernatant was collected and ultracentifugation was performed at 100000 x g for 1 h at 37°C. The resulting pellet was resuspended in the same volume of buffer. Pellet and supernatant samples were diluted with 4x SDS buffer, and run on SDS-PAGE and immunoblotted against α-actin (mouse). G/F actin ratios were quantified and compared with non-tranfected HEK293T cells and JPK pre-treated cells using gel analysis PlugIn in ImageJ/Fiji (Schindelin et al., 2012).

Actin polymerization assay

The actin polymerization assay was performed using Actin Polymerization BiochemKit (Cytoskeleton, BK003) essentially according to the manufacturer's instructions. Briefly, the reactions were carried in dark 96 well plates in 320 μl volume and contained freshly solubilized 1.5 μM pyrene-labeled G-actin, 10 nM Arp2/3 Protein Complex (Cytoskeleton, #RP01P), 400 nM WASP-VCA Domain-GST Protein (Cytoskeleton, #VCG03), 150 nM GST-cortactin or equimolar amount or GST control and 190 nM of untagged caldendrin. All other components were used according to the manual. The rate of actin polymerization was measured by monitoring the change in fluorescence intensity of pyrene-actin using FLUOstar Omega plate reader (BMG Labtech). Intensities were recorded with excitation at 355 nm and emission at 410 nm with 60 s time interval for about 1 hour.

Actin depolymerization assay

In vitro actin depolymerization assay was carried out as recommended by instructions for measuring cofilin-1 activity (Cytoskeleton, #CF01). Fresh pyrene-labeled G-actin was polymerized into filaments as described above using Actin Polymerization BiochemKit (Cytoskeleton, BK003). Depolymerization reactions were performed in 150 μl volume. For the assay, recombinant cofilin-1 was diluted to the final concentration of 5 μM and used in 1:1 ratio with F-actin. Reactions were incubated for 30 min at the RT and ultracentrifuged at 100.000 x g for 1 h to pellet F-actin and associated proteins. Supernatant containing actin monomers and soluble proteins was transferred in a separate tubes and the pellet fraction was diluted in 150 μl of Tris buffer (pH 8.0). Samples were solubilized using 4x SDS loading dye and analyzed by SDS-PAGE and Coomassie blue staining.

TIRF microscopy: in vitro *actin assays*

For all experiments, coverslips and microscope slides were first cleaned by sonication in Milli-Q H_2O for 10 min, followed by successive sonications in acetone and 70% ethanol for 20 min each. Cleaned coverslips were stored in 0.5 M KOH at RT. Before use, coverslips were rinsed with Milli-Q H_2O and dried at 60°C. Flow cells were assembled by attaching the coverslips to the microscope slides using Parafilm that had been cut to form an approx. 5 × 20 mm flow channel. The inside of the flow channel was coated by subsequent incubation with 0.2 mg/ml PLL-PEG-biotin (SuSos AG) for 5 min, 1 mg/ml neutravidin (Thermo Scientific) for 10 min, and 5 mg/ml κ-casein (Sigma) for 10 min. All reagents were diluted in PEM80 buffer (80 mM Pipes·KOH, pH 6.8, 5 mM $MgCl_2$, 0.5 mM EGTA). To obtain actin filaments, actin monomers (Cytoskeleton; 1 mM final, 25% Alexa-561 labeled) were diluted into polymerization buffer (final concentration 10 mM imidazole, 50 mM KCl, 1 mM $MgCl_2$, 100 mM DTT, 0.4 mM ATP, 6 mg/ml glucose, 40 μg/ml catalase, 200 μg/ml glucose-oxidase) and incubated at RT for 20 minutes. The filaments were then added into the flow chamber (25°C, 95% humidity) and allowed to bind for 15 s. Unbound filaments were washed out using polymerization buffer, and spontaneous depolymerization was imaged using TIRF settings (300 ms exposure, 10 s intervals, 300 s duration). The buffer was then replaced by polymerization buffer containing the indicated proteins at different concentrations (3 μM caldendrin, 4 μM cortactin) and the same imaging regime was repeated. Finally, polymerization buffer containing the same amount of caldendrin or cortactin, respectively, and additional 300 nM cofilin (Cytoskeleton) was added in the flow channel and severing by cofilin was imaged as before. Image analysis was done using Fiji. For spontaneous depolymerization, kymographs of single filaments (20 - 40 filaments per conditions) were generated and depolymerization rates were calculated from the slope of the graphs. For cofilin cutting rates, at least 40 filaments in the frame were selected and cuts that appeared in the first 90 s after cofilin addition were counted.

Cell culture and microscopy

Cell culture, transfections, and replating assay

For imaging experiments, cells were grown on 12 mm glass coverslips, for biochemical experiments in T75 culture flasks or 10 cm Petri dishes as described in the experimental model and subject details. Transfection of cells was done using the PolyFect transfection reagent (QIAGEN GmbH, Hilden, Germany), MaxPEI (25000, Polysciences; HEK293T) or Fugene6 (Promega; COS-7) according to manufacturer's instructions, at about 50%–60% confluency. In general, cells were used 48 h (imaging) and 24 h (biochemistry) after transfection.mCherry-cortactin and caldendrin-GFP plasmids were co-transfected into COS-7 cells and cells were re-plated on glass coverslips after 1 day to induce high cytoskeleton dynamics, fixed 4 h thereafter and imaged using Leica SP5 confocal microscope.

Neuronal culture, transfections and lentiviruses

Primary hippocampal rat cultures were prepared as described previously (Kapitein et al., 2010). Dissociated hippocampal neurons from caldendrin $^{+/+}$ and $^{-/-}$ mice were prepared as recently described (Spilker et al., 2016). In brief, hippocampi were dissected from male and female P0 $^{+/+}$ and $^{-/-}$ mice and cells were dissociated after 10 min treatment with trypsin at 37°C. Neurons were plated on plastic μ-dishes (Ibidi) coated with poly-L-lysine (Sigma-Aldrich) at a density of 50000 cells for transfection purposes or for immunocytochemistry on poly-L-lysine coated glass coverslips at a density of 30000 cells per well in DMEM medium (GIBCO, Thermo Fisher Scientific) supplemented with 8% FCS, 1% penicillin/streptomycin. Following attachment, cells were kept in Neurobasal medium (GIBCO) supplemented with 0.5 mM Glutamax, 2% B27, and 1% penicillin/streptomycin (all from GIBCO), at 37°C, 5% CO_2 and 95% humidity. Primary hippocampal mouse and rat cultures were transfected with lipofectamine 2000 (Thermo Fisher Scientific) according to manufacturer's instructions and as described previously (Kapitein et al., 2010). For overexpression cells were transfected for 24-72 h, for the shRNA knock down 48-72 h. For rescue of shRNA effects, jasplakinolide was added at the indicated concentrations during the time of knockdown (48 h). Lentiviral particles for knockdown of caldendrin and cortactin were produced as described previously (Schätzle et al., 2016). For knockdown experiments, 20 μl of virus solution was applied to primary cultures at DIV14 and DIV22. MARCKS-GFP expression was induced by application of 500 ng/ml doxycycline 48-72 h prior to recordings.

BDNF stimulations of primary neurons

Stimulation of BDNF was done by addition of 50-100 ng BDNF in 1 mL medium per well of a 12-well plate for time indicated. For spinning disc microscopy neurons were imaged over 1 h after stimulation. For morphological analysis neurons were stimulated for 2 h and immunostaining was performed as described below using following antibodies: mouse anti-bassoon and rabbit MAP2.

Immunocytochemistry

Cells were fixed in 4% PFA for 10 min at RT and washed three times with PBS, before they were permeabilized in 0.2% Triton X-100 in PBS for 10 min. After thoroughly washing, coverslips were incubated in blocking buffer (BB) for 1 h at RT. Incubation in primary antibodies was performed in BB at 4°C over night. After additional washing in PBS, cells were incubated in secondary antibody dilution in BB for 1 h at RT. Coverslips were rinsed in water and mounted with mowiol. Immunostainings that included phalloidin staining followed a slightly different protocol. Cells were fixed at DIV21 with 4% PFA (Roti-Histofix, Carl-Roth)/ 4% sucrose in PBS for 10-15 min at RT, blocking buffer consisted of 0.1% Triton X-100, 10% horse serum in PBS. After secondary antibody staining, phalloidin-647N (0.165 nM in PBS) incubation was performed at RT for 2.5 h and subsequently at 4°C overnight.

AMPAR surface staining

Primary hippocampal rat cultures DIV14-17 were stimulated with 100 ng/ml BDNF for 2 hours or 50 μM bicuculline for 15 min, washed with pre-warmed medium and immediately fixed with PFA. During the last 30 min anti-GluR1 (extracellular epitope) was applied 1:20 to the medium to stain surface AMPA receptors. Afterward immunostaining for homer, and staining of actin with phalloidin was performed as described above.

Microscopy

Nissl staining and wide field microscopy

Adult male caldendrin $^{+/+}$ and $^{-/-}$ mice were decapited, brains removed and shock frozen. Frontal sections of 40 μm thickness were cut on cryostat and thereafter stained according to Nissl using cresyl violet. Shortly, sections were acidified using 0.05 M acetate buffer (pH 4) for 5 min and then stain in 0.05% cresyl violet acetate solution for 10 min. Afterward sections were differentiated in 0.05 M acetate buffer (pH 4) for 3 min and dehydrated by passing through 50%, 70% and 96% ethanol for 2 min each. Sections were cleared in isopropanol:ethanol (2:1) solution 2 times for 5 min each and 3 times in xylol for 5 min each. Sections were mounted in Entellan (Millipore) onto glass objective slides. Microscopy images were taken on a Zeiss microscope equipped with 1.25x and 20x objective and Leica DFC 500 Camera using Leica LAS software v3.6 with constant exposure times between genotypes.

Widefield fluorescence microscopy

Images for sholl analysis of neurons in primary hippocampal culture were acquired on an Axio Imager.A2 microscope (Zeiss) equipped with a HXP120C light source and a CoolSNAP EZ, 20x air and 40x oil objectives and camera and operated by VisiView 2.0.4 software (all Visitron Systems).

Confocal Microscopy of slices

Images for neuron tracing in hippocampal slices were acquired using HCX PL APO CS 63.0x1.40 oil objective without setting zoom factor using 561 nm excitation (512 px, 8 bit, 400 Hz, 1 μm z steps, 2.081 px/μm resolution, frame average 2). Tiles were subsequently

merged with Leica ASF software and standard settings. Dendritic segments were imaged with equal settings, but 4 x zoom and 0.3 μm z-steps.

FRET assays in COS-7 cells

FRET acceptor bleaching experiments were used to study the dynamic confirmation of caldendrin upon Ca^{2+} binding in living cells. COS-7 cells were grown on μ-dishes (Ibidi) or on glass coverslips in 6-well plates and transfected with YFP-caldendrin-CFP, YFP-CFP tandem construct or YFP and CFP in separate plasmids. Imaging was done in Ringer's solution with or without $CaCl_2$. For increasing intracellular Ca^{2+} concentration cells were stimulated with 1 μM ionomycin and imaged within 5-20 min after this treatment.

Experiments were performed on a SP5 CLSM systems (Leica-Microsystems) equipped with an Argon laser and acousto-optic tunable filters (AOTF), controlled by LAS AF (Leica Application Suite Advanced Fluorescence) software, to choose suitable Argon laser lines. CFP was excited with 458 nm laser line and YFP with 514 nm laser line. YFP was bleached with 514 nm laser line with maximal power setting. All FRET-AB experiments were carried out in humidified chamber at 37°C and 5% CO_2.

FRET efficiency (E_{FRET}) was analyzed using Leica FRET-AB Wizard where E_{FRET} was calculated as $E_{FRET} = (D_{post}-D_{pre})/D_{post}$ with D being donor fluorescence before (pre) and after (post) acceptor bleaching.

To test Ca^{2+} and caldendrin-dependent change in conformation of cortactin, COS-7 cells were transfected with YFP-cortactin-CFP alone or together with caldendrin. Experiments were performed in culturing medium as described above.

In addition, as independent read out of interaction, spectral FRET was measured in cell extracts. HEK293T cells were transfected with constructs expressing YFP-cortactin-CFP fusion protein (CFP as donor and YFP as acceptor) and untagged caldendrin (caldendrin in pcDNA3.1) for the experiment and CFP, YFP for negative control and tandem CFP-YFP for positive control. Cells were lysed with lysis buffer (1xTBS 1% Triton X-100, 10% glycerol and PI) 48 h after transfection. Cell homogenates were pre-cleaned by centrifugation at 12000 rpm for 10 min at 4°C. FRET measurements were recorded on an F-7000 fluorescence spectrophotometer (Uwe Binninger Analytic). Excitation of was done at 370 nm (CFP) and 485 nm (YFP) and emission spectra were recorded at wavelengths between 450-600 nm. The concentration of the CFP, YFP or CFP-YFP fusion proteins in cell lysates was normalized to YFP fluorescence.

FRET assays in neurons

To assess the conformational change of caldendrin upon calcium binding/synaptic activity FRET AB experiments with overexpression of YFP-caldendrin-CFP in primary hippocampal cultures of $cald^{-/-}$ mice were performed. Neurons were transfected DIV11, kept in conditioned medium containing 1 μM TTX and imaged the next day. CFP-YFP tandem and CFP and YFP were used as positive and negative controls, respectively. Photo-bleaching of YFP and FRET measurements was done in individual spines as described above. Same coverslipes were used for measurements in silenced culture and after wash out and stimulation with 50 μM bicuculline.

For testing Ca^{2+} dependent interaction of cortactin and caldendrin in spines, GFP-caldendrin-GFP and mCherry-cortactin were co-transfected in DIV13-16 rat primary neurons. mCherry-GFP tandem was used as positive and mCherry and GFP expressed from the separate plasmids as negative controls. Experiments were performed as described above. GFP was excited with 488 nm laser line and mCherry with 561 nm laser line. mCherry was bleached with 561 nm laser line with maximal power setting. Measurements were performed within maximum 1 hour after bicuculline stimulation.

Protein turnover and FRAP experiments

DIV20/21 mouse and DIV30 rat hippocampal cultures were treated with 50 μM bicuculline for 5 min and 15 min, respectively, in culturing medium and fixed with 4% paraformaldehyde (PFA) directly afterward.

Protein dynamics in spines was analyzed in DIV11-13 primary hippocampal cultures of $cald^{+/+}$ and $^{-/-}$ mice. Live imaging was performed using Leica SP5 microscope equipped with a 5% CO_2, 37°C humidified chamber and using the Leica software inbuilt FRAP wizard. Imaging settings were as follows: 63x objective (HCX PL APO CS 63.0x1.40 oil objective) and 4x zoom, 8bit, 512px, 8.3px/μm. Images were taken in 5 s (FRAP) or 10 s (basal) intervals. For FRAP experiments photo-bleaching of the ROI was achieved with 3-5 continues scans with maximum laser power at 488 nm after 5 baseline images. Afterward 25 post-bleach images with 5 s interval were taken. For rescue FRAP experiments DIV11-13 mouse hippocampal cultures were treated with 50 μM bicuculline for 5 min and imaged 8 h afterward.

Fluctuations of spinous actin under basal conditions was measured in individual spines in hippocampal primary cultures DIV12 transfected with GFP-actin alone or co-expressed with mRuby2.

The average GFP value per spine was used to normalize each trace and the sum of absolute values between each 2 consecutive time points was calculated and defined as total fluctuations.

FRAP efficiency was calculated using Fiji. ROIs were placed on individual (bleached) spines, on a non-bleached dendritic stretch as control and in the background. The intensities were measured using 'Plot z axis profile' option. Subsequently, intensity values for spines were background subtracted per time point, normalized to the dendritic control and normalized to the first pre-bleach value.

Spinning disc microscopy

Spinning disc recordings were acquired with a Yokogawa CSU-X1-A1NeE unit mounted on a Nikon Eclipse-Ti microscope. Samples were recorded with a Plan Apo VC 100 ×, 1.4 NA oil objective using a 491-nm laser (100 mW, Cobolt Calypso) for excitation and a ET-GFP (49002, Chroma) emission filter. The motorized stage (ASI, MS-2000-XYZ with piezo top plate) together with the Nikon perfect focus system allowed performing multi-position imaging over time. MetaMorph 7.6.4 software (Molecular Devices) was used to

control the Evolve 512 EMCCD camera (Photometrics) and all motorized microscope parts. Neurons were recorded in full conditioned medium and maintained in a Tokai Hit Stage Top Incubator (INUBG2E-ZILCS) at 37°C with 5% CO_2.

STED Imaging

STED images of phalloidin-Alexa647 and cortactin-Abberior Star 580 were acquired on a Leica TCS SP8-3X gated STED microscope equipped with a pulsed 775 nm depletion laser and a pulsed white light laser (WLL) for excitation. For acquiring images the Leica objective HC APO CS2 100x/1.40 oil was used. Fluorescence of respective channel was excited by the WLL at 650 nm (phalloidin; STED and confocal), 488 nm (MAP2; confocal mode) and 561 nm (cortactin; STED and confocal), respectively. For STED imaging emission was acquired between 660 - 730 nm for Atto647N and 580-620 nm for Abberior Star 580. The detector time gates for both STED channels were set from 0.5 - 1 ns to 6 ns. Both dyes were depleted with 775 nm. Images were taken as single plane of 1024x1024 pixels and digital zoom factor 5, 600 lines per second and line averaging of 16.

Glutamate uncaging experiments

Organotypic hippocampal slice cultures

Organotypic hippocampal slice cultures (OHSC) were prepared from male and female P9 *cald*$^{-/-}$ mice and *cald*$^{+/+}$ littermates as described previously (Gogolla et al., 2006). Mice were decapitated, brains removed, placed in preparation medium (HAME-01 Prep Medium, Cell Concepts, Umkirch, Germany) and hippocampi dissected under a binocular. Perpendicular slices of 350-400 μm thickness were cut using a McIlwain tissue chopper (Mickle Laboratory Engineering, Surrey, UK). After carefully separating the slices in fresh preparation medium, only excellent quality slices were transferred onto millicell membranes (4 slices per membrane, Merck Millipore) placed in 6 well-plates with pre-warmed and CO_2 equilibrated 1 mL OHSC medium. Slices were cultured at 37°C, 5% CO_2, humidity. Feeding of slices was performed by exchanging 0.9 ml of medium at DIV2 and thereafter every 3 days.

Single cell electroporation

At DIV5, individual CA1 neurons were transfected by single-cell electroporation at an upright microscope (Dodt contrast) as described previously (Wiegert et al., 2017). Single-cell electroporation was conducted in extracellular solution containing (in mM): 145 NaCl, 10 HEPES, 25 D-glucose, 2.5 KCl, 1 $MgCl_2$, 2 $CaCl_2$ (pH 7.4, 318 mOsm). Plasmids were diluted (30 ng syn-mRuby2 or 40-50 ng syn-eYFP) in potassium-based intracellular solution containing (in mM): 135 K-gluconate, 0.2 EGTA, 4 $MgCl_2$, 4 Na_2-ATP, 0.4 Na-GTP, 10 Na_2-phosphocreatine, 3 ascorbate, 0.02 Alexa Fluor 594, and 10 HEPES (pH 7.2). Neurons were transfected by 50 hyperpolarizing pulses (−12 mV, 0.5 ms, at 50 Hz) delivered by an Axoporator 800A (Axon Instruments). After transfection the slices were placed back in their original culturing medium, for morphology analyses slices were fixed in 4% PFA/ 4% sucrose one day after and mounted with mowiol. For two-photon glutamate uncaging experiments slices were used 2 to 4 days after electroporation.

Two-photon glutamate uncaging

Two-photon glutamate uncaging was performed on an Olympus FV1000 upright microscope controlled by FluoView software. Excitation was provided by a pulsed Ti::sapphire laser (Mai Tai, Spectra Physics) tuned to 920 nm. Fluorescence was collected through an Olympus XLPlanN 25x MP, 1.05 NA water dipping objective and a 495-540nm emission filter. Slices were submerged in recirculating bubbled (95% O_2, 5% CO_2) Mg^{2+} free ACSF (in mM: 119 NaCl, 26.2 $NaHCO_3$, 11 $C_6H_{12}O_6$, 1 NaH_2PO_4, 2.5 KCl, 3 $CaCl_2$, pH 7.4, 30-32°C) containing 2.5 mM MNI-caged-L-glutamate (Tocris) and 0.001 mM TTX (Tocris). Spines on the secondary or tertiary branch of oblique dendrites were targeted for potentiation. After imaging of a 15 minute baseline, glutamate was uncaged by tuning the laser to 720 nm and application of 60 pulses, 1 ms at 1 Hz. Laser intensity at the back focal plane ranged approximately between 15 and 20 mW. Following uncaging the spine volume was monitored for 1 h.For analyses spine size was estimated by the integrated intensity within a circular ROI surrounding the spine head using Fiji. Background was subtracted by measuring the intensity within an equally sized ROI away from the recorded dendrite. To estimate changes in spine size, the fluorescence from individual spines was normalized to the fluorescence during a 15 minute baseline. Spines that did not respond to the uncaging stimulus were excluded (< 20% increase 2 min after uncaging).

Electrophysiology in acute hippocampal slices

Field recordings

Hippocampus from 8-11 weeks old male mice (*cald*$^{+/+}$ mice and *cald*$^{-/-}$ mice) were cut using a vibratome (LeicaVT1000S, Nussloch, Germany) into 350 μm thick slices. These hippocampal slices were incubated for 2 h in carbogenated (95% O_2 / 5% CO_2) artificial cerebrospinal fluid (ACSF, containing in mM: 110 NaCl, 2.5 KCl, 2.5 $CaCl_2 \cdot 2H_2O$, 1.5 $MgSO_4 \cdot 7H_2O$, 1.24 KH_2PO_4, 10.0 glucose, 27.4 $NaHCO_3$, pH 7.3) at 31 ± 1°C. Field excitatory postsynaptic potentials (fEPSPs) were evoked by stimulation of CA1 Schaffer-collateral fibers with biphasic rectangular current pulses (200 μs/polarity, frequency 0.033Hz) in a range of 4-5V through ACSF filled glass capillary microelectrodes (3-5 MΩ). fESPSs were recorded using ACSF filled capillary microelectrodes and amplified by an extracellular amplifier (EXT-02B, npi, Germany) and digitized at a sample frequency of 5 kHz by a Digidata 1401plus AD/DA converter (CED, England). Stimulation strength was adjusted to 40%–50% of the maximum fEPSP-slope values. L-LTP was induced by tetanization consisting of three 1 s stimulus trains at 100 Hz with a 6 min inter-train interval. JPK was dissolved in DMSO, and diluted in ACSF to the final concentration 50 nM. It was washed in 30 min before tetanization and washed out 50 min after tetanization. Input/Output curve were tested by different stimulus intensities (V). Picrotoxin was applied in a concentration of 100 μM. Paired-pulse facilitation was measured by different interpulse intervals (ms). LTD was induced by low frequency stimulations (900 stimuli at 1 Hz).

Patch-clamp and calcium fluxes recordings

Transverse 400 μm slices from the right hippocampus of adult *cald*$^{+/+}$ and $^{-/-}$ mice (10-15 weeks old) were cut with a vibratome (Leica VT1000S) in ice-cold ACSF solution. Slices were incubated at 34°C for 25 min and subsequently held at room temperature.

For measuring miniature excitatory postsynaptic currents (mEPSCs) the extracellular solution contained in mM: 124 NaCl, 4.9 KCl, 2 $MgSO_4$, 2 $CaCl_2$, 1.2 KH_2PO_4, 25.6 $NaHCO_3$, 20 glucose, 1 μM TTX, 10 μM bicuculline and 10 μM APV. The intracellular solution contained in mM: 140 potassium gluconate, 10 EGTA, 10 HEPES, 2 $MgCl_2$, 1 $CaCl_2$, 4 NaATP and 0.4 GTP.

For measuring the NMDA to AMPA ratio the extracellular solution contained in mM: 124 NaCl, 4.9 KCl, 2 $MgSO_4$, 2 $CaCl_2$, 1.2 KH_2PO_4, 25.6 $NaHCO_3$, 20 glucose and 10 μM bicuculline. The intracellular solution contained in mM: 120 $CsMeSO_4$, 30 TEA, 10 EGTA, 5 $MgCl_2$ 10 HEPES, 4 NaATP and 0.4 GTP. A stimulation electrode was placed in the stratum radiatum to stimulate the Schaffer collaterals. The stimulation strength was adjusted to get an EPSC at −90 mV of around 200 pA. Neurons were held at −90 mV for measuring AMPA-mediated-EPSCs and at +50 mV for measuring NMDA-mediated-EPSCs.

For measuring calcium fluxes in CA1 pyramid spines a commercial two-photon laser-scanning Femto2D microscope from Femtonics (Budapest, Hungary) was used. Laser pulses at 810 nm were provided by a Ti:Sapphire femtosecond laser (Cameleon Ultra I, Coherent). Cells were filled with Alexa Fluor 594 and Fluo 5F through the patch pipette. For measuring Ca^{2+} signals, green (Fluo 5F) and red (Alexa Fluor 594) fluorescence were collected during 500 Hz line scans across the spine head after a short current injection to the soma (1 nA for 5 ms). Fluorescence changes were quantified as the increase in green fluorescence normalized to the average red fluorescence (ΔG/R). Fluorescence was collected through the objective (60 × 1.0 NA, Olympus) and the oil immersion condenser (1.4 NA, Olympus) with two pairs of photomultipliers. The composition of the intracellular solution for these experiments was in mM: 130 potassium gluconate, 20 HEPES, 2 $MgCl_2$, 2 Mg-ATP, 0.3 Na-GTP, 0.25 Fluo-5F and 0.1 Alexa 594.

Patch pipettes (3–5 MΩ) were pulled from thick-walled borosilicate glass tubing. Recordings were performed with an EPC9 patch-clamp amplifier. Data were acquired and stored using Patchmaster and analyzed with Fitmaster and Minianalysis.

Behavior

Cannula implantation and drug delivery

Caldendrin $^{+/+}$ and $^{-/-}$ male littermates were acutely injected with JPK according to the method of intrahippocampal injection described previously (Albrecht et al., 2013). Mice were anesthetized with intraperitoneal sodium pentobarbital injection (50 mg/kg, Sigma-Aldrich, Seelze, Germany) and placed on a stereotactic frame (World Precision Instruments, Berlin, Germany). A bilateral 26 G guide cannula (C235GS-5-2.0/SPC, Plastic One Inc., USA) was stably implanted targeting the CA1 area of the dorsal hippocampus. The guide cannula placement was anterioposterior (AP) −1.94 mm; mediolateral (ML) ± 1 mm from Bregma and dorsoventral (DV) 1.5 mm below pedestal from the brain surface. Guide cannulae were secured and closed with dummy cannulae to prevent clogging and were covered with dust caps. Mice were single caged and allowed to recover from surgery for 12 days before drug infusion and behavioral testing. On the day of testing, mice were briefly anesthetized with isoflurane and 33 G internal cannulae were inserted to extend 0.2 mm beyond the tip of the guide cannulae (total depth 1.7 mm). JPK was dissolved in 0.9% saline at a final concentration of 50 nM. Mice received bilateral infusions of either JPK or 0.9% saline serving as vehicle (VEH) (1.5 μl/side at 0.5 μl/min), 30 min before the first exposure to the test apparatus. After the completion of the behavioral task injection sites were verified histologically. To this end mice were infused with 0.5 μl/side (1:10 in 0.9% saline) red retrobeads (Lumafluor Inc., USA) according to the infusion protocol described above and two days later were transcardially perfused with 4% PFA. Brains were snap frozen in liquid nitrogen and 30 μm-thick coronal sections were made and analyzed under Leica DMI 6000 CS fluorescence microscope (Leica Microsystems, Germany).

Novel object recognition

The effect of JPK administration on hippocampus dependent memory was assessed using a novel object recognition assay. 3-6 month-old male mice were divided into four groups, *cald*$^{-/-}$ infused with VEH (9) and JPK (9) and *cald*$^{+/+}$ infused with VEH (9) and JPK (8). Training and testing were done in an open field square arena made out of gray plastic (50 cm x 50 cm). To ensure a low basal stress level, experimental animals were briefly handled before the behavior paradigm. 30 min after infusion, mice were habituated in the empty arena for 20 min. Then, two identical objects were introduced to the maze and mice were allowed to explore the objects, in two training sessions, each lasting 20 minutes. In the memory test phase, 2 h after the end of the second training, one familiar object was replaced with an object that was unfamiliar to the animal (novel object). The object positions were kept constant between trials, but randomized between animals to exclude potential spatial bias. Object exploration was measured and recorded via the ANY-maze (Video Tracking System, version 4.50, Stoelting Co., Wood Dale) and "object exploration" was defined as object-directed movement at a distance ≤ 2 cm from the object and/or touching it with the nose. The experimental design and layout is shown in the Figure S8C. Data are expressed as novel recognition index (RI), i.e., the time spent investigating the novel object relative to the total object investigation (time at novel + time at familiar object) and statistically tested against chance level (0.5), reflecting equal exploration of both objects.

Open field and elevated plus maze tests

Open field and elevated plus (EPM) maze tests were performed as described previously (Albrecht et al., 2013). In short, for the first test mice were placed in the center of an open field arena and were allowed to freely explore the area at low light conditions (10 lux). Mice behavior was recorded online via the ANY-maze video tracking system. The total traveled distance during the test session was

analyzed, and the time spent in the center of the open field (10 cm x10 cm) was determined to assess anxiety-related behavior. Time spent in open and closed arms in EPM test were recorded at similar conditions during a 5 min test.

QUANTIFICATION AND STATISTICAL ANALYSIS

Analysis of dendritic morphology

In hippocampal slices only pyramidal neurons of CA1 without close by transfected other cells were included in the analysis. Equal distribution of cell position for knockout and wild-type slices was given and analysis was done by a researcher blind to mouse genotype. Neurons were traced using the simple neurite tracer plugin (Longair et al., 2011) of the Fiji software in z stacks. Measurement of dendritic length and Sholl analysis (dendritic intersections with concentric circles around some in 10 μm distance steps) was done using the above mentioned plugin.Analysis in primary culture was performed in widefield fluorescence images using the same plugin or by drawing concentric circles around the soma and manually counting the number of intersections.

3D reconstructions and spine analysis in Imaris

Spine characteristics in control or BDNF treated primary neurons were analyzed using Imaris software (Bitplane, Belfast, United Kingdom). 0.4 μm stacks imaged at Leica SP5 confocal microscope were imported into Imaris 7.7.1 and a Gaussian blur filter with 1 px (0.12 μm) filter width was applied in the GFP channel before reconstruction. Dendrites were built using the auto-path option of the filament tracer and default settings. Detection of spines was done using following settings: 0.15 μm minimal head size, 0.6 μm maximum length, seed point threshold approx. 10, no branched spines were allowed. To rebuild spine diameters the shortest distance from distance map was used. Spine detection was manually corrected if necessary. Classification of spines into stubby, mushroom-like and filopodia was performed using the Imaris XTension classify spines with following definitions: stubby: spine length < 1 μm; mushroom: spine length < 3μm and spine head width ≥ 0.5 μm; filopodia: true.

Analysis of spine morphology in organotypic hippocampal slices was performed on deconvolved images. Confocal stack images of dendritic segments of CA1 pyramidal neurons expressing mRuby2 in hippocampal slice cultures were deconvolved using Auto-QuantX3 (Media Cybernetics) as follows: adaptive point spread function (PSF), blind deconvolution (with theoretical PSF) in two dimensions, one iteration and medium noise suppression for mRuby2. Afterward a 1 px 2D Gaussian blur filter was applied in Fiji and resulting images used for 3D reconstruction and analysis using Imaris 8.1. Dendrites were built using the auto-path option of the filament tracer and default settings. Detection of spines was done as described above. Classification of spines into stubby, mushroom-like and filopodia was performed using the Imaris XTension 'classify spines' according to the following definitions: spines: length(spine) < 1 or (length(spine) < 3 and max_width(head) > = 0.3), filopodia: true.

Quantification of synaptic puncta

OpenView software was used to analyze cortactin staining intensities in synapses (Tsuriel et al., 2006). Shortly, bassoon positive puncta were identified in maximum projections of confocal images by setting regions of interest around local intensity maxima (Box_puncta_Ex). Cortactin was measured within square areas containing identified bassoon puncta, if cortactin also showed local intensity maxima (match set). Size of areas was defined as boxes with 16 px length and width, corresponding to approx. 1 μm). Surface AMPAR was measured within square areas containing identified homer puncta if AMPAR also showed local intensity maxima (match).

Spine numbers in *cald*$^{+/+}$ and $^{-/-}$ cultures were counted manually by a researcher blind to experimental group in maximum projections of confocal images. Only spots in close proximity to the dendrite with clear overlapping fluorescence of shank2 and synaptophysin were counted independent of spot size. Spines were counted on dendritic stretches of approximately 30 μm length. Spine numbers for caldendrin overexpression and knockdown experiments were counted manually along approx. 30 μm long dendritic segments in overlay images of GFP, β-galactosidase-HA and synapsin fluorescence by a researcher blind to experimental group.

Analysis of actin distribution in spine heads

The distribution of actin in the heads of mushroom-like spines of DIV14 primary hippocampal neurons of *cald*$^{+/+}$ and $^{-/-}$ mice was analyzed in STED images of 2 independent phalloidin-Atto647N stained cultures under basal conditions and after 5 min of bicuculline stimulation (50 μM). Line scan analysis from the tip of the spine (presynaptic bassoon staining as reference) to the spine neck was performed using Fiji option 'plot profile'. Intensities of individual spines were normalized to the length of the spine head and to the highest intensity values. The distribution of actin within the spine head was analyzed using a custom-written script in MATLAB (R2015a, MathWorks, Inc). In short, a circular ROI was placed on the middle of the spine head completely covering the spine head. The ROI was divided into 12 equally sized sectors (4 quadrants each subdivided into 3 sectors) with the spine neck always facing the same direction. Phalloidin-Atto647N intensities were measured in each of the sectors based on pixel intensities (16-bit) and normalized to the total amount of Phalloidin-Atto647N per spine head. These values were plotted in a color code. Additionally, for each quadrant the ratio of the inner most sector versus the other 2 combined were calculated and plotted in the rose plots as actin enrichment ratios. At last, for each spine head we estimated the weighted center of mass including pixel values of all the pixels within the ROI. To compare spines, we normalized the coordinates (−100 to +100) of the center of mass to the ROI size with coordinates 0,0 as center of the spine head.

Statistical analysis

Statistical analysis was performed in Prism 6.05 (GraphPad, La Jolla, CA, USA). The type of parametric test used for each experiment and significant levels are stated in the corresponding figure legends. The reported n numbers correspond to spines, protrusions, dendritic segments, neurons, analyzed field of views/images, actin filaments, animals, or experimental replications as indicated. For experiments that include samples taken mice animal numbers are given additionally in the figure legends. Values are reported as mean ± SEM throughout the manuscript.

Data quantified from cell culture experiments (cell lines and primary culture) were obtained from at least 3 independent experiments/culture preparations, *in vitro* actin assays (TIRFM) are from 3 independent experiments.

DATA AND SOFTWARE AVAILABILITY

Requests for data and software should be directed to the Lead Contact Michael R. Kreutz and will be made available upon reasonable request.